A new type of (TiZrNbTaHf)N/MoN nanocomposite coating: Microstructure and properties depending on energy of incident ions

A.A. Bagdasaryan[a,b], A.V. Pshyk[b,*], L.E. Coy[b], P. Konarski[c], M. Misnik[c,d], V.I. Ivashchenko[e], M. Kempiński[b,f], N.R. Mediukh[e], A.D. Pogrebnjak[a], V.M. Beresnev[g], S. Jurga[b]

[a] *Sumy State University, 2, Rymsky Korsakov Str., 40007, Sumy, Ukraine*
[b] *NanoBioMedical Centre, Adam Mickiewicz University, 85, Umultowska Str., 61-614, Poznań, Poland*
[c] *Tele & Radio Research Institute, 11, Ratuszowa Str., 03-450, Warsaw, Poland*
[d] *Department of Atomic, Molecular and Optical Physics, Faculty of Applied Physics and Mathematics, Gdańsk University of Technology, Poland*
[e] *Frantsevich Institute for Problems of Materials Science, National Academy of Sciences of Ukraine, 3, Kryzhanovskogo Str., 03680, Kyiv, Ukraine*
[f] *Faculty of Physics, Adam Mickiewicz University, Umultowska 85, 61-614, Poznań, Poland*
[g] *Kharkiv National University, Svobody Sq., 4, 61022, Kharkiv, Ukraine*

ARTICLE INFO

ABSTRACT

A novel (TiZrNbTaHf)N/MoN nanocomposite coatings, which consist of the nitride of the high-entropy alloy and the binary nitride, were synthesized by vacuum-arc deposition at various substrate biases. The elemental composition, chemical bonding state, phase structure, microstructure and mechanical properties of the coatings were studied by high-resolution experimental methods: SIMS, GDMS, XPS, XRD, HR-TEM and nano-indentation. It was found that the chemical state of the (TiZrNbTaHf)N/MoN coatings has a complex nature, which consist of a mixture of nitrides of constituting elements. It was also shown that the coatings are based on B1 NaCl-structured γ-Mo_2N-phase with a mixture of crystallographic orientations (111), (200), (220) and (311) together with the B1 NaCl-structured (TiZrNbTaHf)N solid-solution phase. First-principles calculations demonstrated that the metal sub-lattice of the (TiZrNbTaHf)N solid solution can be based on $Ti_{1-x}Hf_yTa_{1-x-y}$, $Zr_{1-x}Hf_yTa_{1-x-y}$, $Zr_{0.25}Ti_{0.25}Ta_{0.5}$ ternary alloys, which have the lowest mixing energy. The HR-TEM results showed that the nanocomposite nitride coatings have nano-scale multilayer structure with modulation periods ranged from 20 nm to 25 nm. The maximum hardness of approximately 29 GPa demonstrated the coating deposited at a higher energy condition (−200 V) with the thinnest modulation period of bilayer of 20 nm (15 nm of (TiZrNbTaHf)N and 5 nm of Mo_2N).

1. Introduction

The recent breakthrough in the last century in engineering materials is design of nanocomposite coatings, which possess superior mechanical and chemical properties, such as high hardness, stiffness, wear resistance, low coefficient of friction, low thermal conductivity etc., in contrast with single layer coatings [1–15]. Such nanocomposite materials are nano-multilayer composites, which have large amount of two or more separated nanocrystalline phases with different elastic modulus and lattice parameters. In order to obtain multilayer coatings with superior functional properties, it is important to adjust carefully their elemental composition and modulation wavelength. It was found that the optimum properties occurs in multilayer coatings with bilayer period Λ in the range of 4–50 nm depending on elemental composition and deposition conditions [16,17].

Nanocomposite architecture allows to achieve excellent functional properties, especially high hardness and low coefficient of friction. There are several hardening mechanisms acting at the same time but at different degrees in the multilayer coatings. First, the hardness alteration could be due to the hindering of dislocation across the layer interfaces. Also, if the constituent layers with different lattice parameters are grow epitaxially, the resulting coherence stress field at the interfaces act as obstacles for dislocation movements [18–20]. Few publications showed another mechanism of hardening, known as Orowan strengthening, which act in structures with nanometer modulation wavelength [21,22]. The improvement in hardness according to this effect occurs at the expense of the precipitation, stopping of dislocation and formation of obstacles, such as "Orowan loop". Despite the great variety of strengthening mechanisms in multilayer structures, the overall hardness enhancement originates from contributions of all

mechanisms. In addition, the effects acting in single-layer coatings, especially in multi-principal elements alloy, such as Hall-Petch effect, solid solution hardening, should be taken into account [23].

In the last decade, it has developed a new approach to designing engineering materials that possess a wide range of unique properties, high-entropy alloys (HEAs) or multi-principal elements alloys (MPEAs). There are two major definitions of HEAs: based on the composition and on the configurational entropy [24–28]. According to *D.B. Miracle* et al. [25], HEAs are the alloys, which contain at least 5 constitutional elements with an atomic percentage between 5 and 35%. Moreover, these alloys can be defined as materials maximum value configurational entropy of which is 1.61 R (where R is the gas constant, 8.314 $j \times k^{-1} \times mol^{-1}$) and minimal value is 1.36 R. In accordance with these definitions, the basic concepts of HEAs is high entropy of mixing, which can promote the stabilization of a disordered solid solution (SS) and prevent the formation of ordered compounds, like intermetallics (IM) due to the lattice distortion effect and sluggish diffusion, which can be explained by kinetic theory [26].

Since the appearance of the first studies of HEAs [29,30], more than 1000 scientific works have been published to date. The relationship between microstructure of the new alloys, which can include SS (with BCC, FCC and HCP structures), IM and even amorphous state [31–33] and their physical properties was investigated [34–36]. It was shown that the HEAs possess different outstanding functional properties, like superconductivity with transition temperature T_c = 7.3 K [37], high level electrical resistivity [38], high saturated magnetization [39,40], high corrosion resistance [41–43], good hydrogen storage properties [44–47]. Moreover, HEAs were used as a template for graphene production [48], high-entropy steel and transformation-induced plasticity-assisted dual-phase high-entropy alloys [49–52]. For achievement superior mechanical behavior and thermal stability HEAs were alloyed by N, C, O and B, like: (TiHfZrVNb)N [53], (AlMoNbSiTaTiVZ)N [54], (TiVCrZrHf)N [55], (TiTaCrZrAlRu)N [56], (CrTaTiVZr)N [57], (TiZrNbNfTa)C [58], (MgNiCoCuZr)O [59], (AlCrTaTiZr)O [60], (MgCoNiCuZn)O [61], $CuCoNiCrAl_{0.5}FeB_x$ [62] and others [63–67].

Since the appearance of first publication by Koehler, the variety of different type of multilayer composites, like metal/metal (Ni/Ti, Co/Ni, Fe/Ni [68–70]), ceramic/metal (TiN/Ag, Al/AlN, NbN/Ag, Ta/TaN [71–74]) and ceramic/ceramic (CrAlSiN/TiVN, AlCrSiN/AlCrSiON/AlCrO, TiN/TiAlN [9,17,75]) have been intensively investigated. Recent papers have showed the possibility of using different type of composites based on HEAs with intrinsic multilayer architecture, like: AlCoCrCuFeNi/Mg [76], (TiHfZrVNbTa)N + DLC [77], (FeCoNiMnCr) +MeC [78], TiAlSiCN/MoSeC [79]. However, the research work devoted to the composites with a HEA layer is still very limited. The only pure metals [76] and carbide interlayers [77–79] have been studied, assuming that the preparation of intermediate nitrides, will affect the Nitride based HEAs. Nevertheless, although it is worth to assume a large diffusion due to the complex stoichiometry of HEAs, especially in similar interfaces, such as in case of Metal-Nitride/Metal-Nitride, these effects have remain unexplored.

It is well known, that the deposition parameters, like temperature of deposition, energy of incident particles, pressure of working gas and others have a significant influence on structural state and overall properties. In our work we developed and investigated a novel (TiZrNbTaHf)N/MoN nanocomposite coatings, which deposited by vacuum arc deposition under different energy conditions. The chemical stability and growth of such complex nanocomposites have been poorly studied. Moreover, the influence of overall ions deposition energy on crystallization process and as a result on interaction between nanolayers should be taken into account and analyzed in order to avoid malfunction of nanocomposite coatings. Clearly, the understanding of microstructural features of such nonhomogeneous complex systems is essentially needed in order to move further toward the improvement of the physical properties of high-entropy based nanocomposite thin films.

This article contributes to the gaining of knowledge about the growth mechanism, structural evolution and functional properties of a novel (TiZrNbTaHf)N/MoN nanocomposite nitride coatings based on the high entropy alloy. In order to achieve this aim, six transition metals Ti, Zr, Nb, Hf, Ta and Mo are selected due to the their similar electronic configuration, which is favored by the octahedral grouping of the metal atoms around a central nitrogen atom, which will allow to achieve a single-phase stable structure.

2. Experimental methods

2.1. Growth and characterization

The five-element TiZrNbTaHf cathodes were obtained by vacuum-arc melting method. Ingots were melted at least six times to achieve necessary compositions homogeneous. All the samples have been prepared by vacuum-arc deposition in "Bulat-6" chamber. The deposition was carried out from the two different cathodes (1 − TiZrNbTaHf alloy, 2 − Mo), diametrically opposed to the substrate holder during continuous rotation of the holder during 1 h. Steel discs and plates (12H18N9T steel – C ≤ 0.12 wt %; Si ≤ 0.8 wt %; Mn ≤ 2.0 wt %; Cr – 17 ÷ 20 wt %; Ni - 8 ÷ 11 wt %; Ti < 0.8 wt %.) with Ø = 45 mm and thickness of 4 mm were used as a substrate. The working gas pressure used during deposition was 0.53 Pa while a negative bias of −100, −200 and −300 V was applied to the substrate (see Table 1). The temperature of deposition was 400 °C.

The X-ray photoelectron spectroscopy (XPS) measurements were performed in UHV conditions using the monochromatic Al Kα X-Ray source and Sphera II photoelectron energy analyzer (Scienta Omicron). All measurements were made in the ultra-high vacuum chamber at a pressure around 10^{-9} mbar. The spectra were taken at 20 eV pass energy and 0.1 eV resolution.

SIMS measurements were done with the use of 5 keV Ar^+ ion beam. SIMS analyser model SAJW-05 is equipped with Physical Electronics 06-350E ion gun and QMA-410 Balzers quadrupole mass analyser with 16 mm diameter rods.

Glow discharge mass spectrometry (GDMS) analysis was conducted with a SAWJ-01 instrument and SRS-300 quadrupole mass analyzer with 6 mm diameter rods. The 1.8 kV DC glow discharge voltage was applied and Ar working pressure was 0.2 Torr.

The structure and elemental composition was analyzed using Scanning electron microscopy (SEM JEOL 7001TTLS) with Energy dispersive X-ray spectroscopy. The electron transparent lamellas of the coatings for TEM measurement were prepared using a focused ion beam (FIB) operating with Ga ions. High-resolution transmission electron microscope (HRTEM JEOL ARM 200F) operating at accelerating voltage of 200 kV was used to image the microstructure of the coating and evaluating of thickness period of multilayers. The microscope was also equipped with an EDX detector used to determine the distribution of the elements.

The crystal structure was characterized by X-ray diffractometer PANalytical using filtered Cu-Kα radiation (1.5418 Å) with PIXcel 3D detector in Bragg-Brentano geometry. Spectra were recorded in continuous scanning mode at room temperature (300 K), with the 2θ ranging from 20.0° to 80.0° and scanning step was 0.006°. Data were processed in the PANalytical X'Pert software.

Table 1
Experimental conditions.

№	Coatings	I, A	U_{sb}, V	P_{N2}, Pa
1	(TiZrNbTaHf)N/MoN	90/150	−100	0.53
2	(TiZrNbTaHf)N/MoN	90/150	−200	0.53
3	(TiZrNbTaHf)N/MoN	120/140	−300	0.53

The nanoindentations were performed at room temperature on (TiZrNbTaHf)N/MoN coatings using Hysitron TriboIndenter 950 equipped with a Berkovich diamond tip TI-0039 (conical angle 142.3° and 100 nm tip radius) calibrated against the fused silica sample. In order to measure the hardness and reduced elastic modulus of the coatings at different depth, the multiple load function in the form of trapezoidal sinus was applied to the indenter with continuously increasing load up to a maximum 10 mN load. The measurements were repeated several times. The hardness and the elastic modulus were evaluated using the standard procedure proposed by Oliver and Pharr [80].

The elastic modulus of the coatings was calculated using the following formula [80]:

$$\frac{1}{E_r} = \frac{1 - \nu^2}{E} + \frac{1 - \nu_i^2}{E_i}, \tag{1}$$

where E_r – effective Young's modulus of coating material, E and ν – Young's modulus and Poisson's ratio of coating material, E_i and ν_i – Young's modulus and Poisson's ratio of the Berkovich diamond indenter (E_i = 1140 GPa and ν_i = 0,07), respectively.

2.2. Computational details

We considered the 8 atoms cubic cells to model $Zr_xTi_yTa_{1-x-y}N$, $Zr_xHf_yTa_{1-x-y}N$ and $Ti_xHf_yTa_{1-x-y}$ (x, y = 0.0, 0.25, 0.5, 0.75 and 1.0) solid solutions (alloys) with the B1 structure (space group Fm-3m, No. 225). These cells were used in first-principles calculations that have been carried out carried using the Quantum-ESPRESSO code [81]. The details of the calculations can be found in our previous work [63], therefore, we note only the following main approaches. In particular, Vanderbilt ultra-soft pseudo-potentials were used [82]. For exchange-correlation energy, the generalized gradient approximation (GGA) of Perdew et al. [83] was employed. The structures were optimized by using the Broyden–Fletcher–Goldfarb–Shanno (BFGS) algorithm [84]. For Hf and Ta the 4f states are not considered as the valence states, because they are completely filled and chemically inert. The mixing energy of an alloy (E_{mix}) was:

$E_{mix}(Me_xMe_yMe_{1-x-y}N) = E_{tot}(Me_xMe_yMe_{1-x-y}N) - x \times E_{tot}$ (MeN) $- y \times E_{tot}$ (MeN) $- (1-x-y) \times E_{tot}$ (MeN), where Me, Me, Me = Ti, Zr, Hf and Ta.

3. Results

3.1. Elemental composition and chemical bonding

Before analyzing of elemental composition by SIMS and GDMS methods, it will be useful to analyze the chemical bonding states of (TiZrNbTaHf)N/MoN nanocomposite coatings by means of XPS.

The XPS survey spectrum (see Fig. 1 (a)) contains peaks, which associated with titanium, zirconium, molybdenum, niobium, tantalum, nitrogen and oxygen. Carbon (peak at 284 eV) and oxygen (peak at 532 eV) peaks are due to the contamination of the coating by the small amount of residual gases in vacuum chamber during the deposition and contamination of the coating surface by ambient atmosphere [85]. For analyzing, we selected Ti2p, Mo3d, Zr2p, and Nb3d core-level peaks due to the absence of overlapping effects of these peaks with the other constituent elements of the coating. Importantly, Hf was detected in the coating as well, but the intensity of Hf4f and Hf4p$_{1/2}$ peaks was very low and inappropriate for analysis, while the Hf4s may overlap with O1s.

The Zr3d spectrum (Fig. 1 (b)), containing peaks corresponding to the spin-orbit split 3d$_{3/2}$ and 3d$_{5/2}$ electrons, was de-convoluted into 2 doublet components: (1) peaks at 183.04 eV and 179.42 eV, respectively, and (2) peaks at around 184.44 eV and 181.89 eV, respectively.

According to the literature data, the energy position of the first component can be due to ZrN$_x$ bonds, while the second component is attributed to ZrO$_2$ bonds in the coating [86].

The Ti2p XPS spectrum was de-convoluted into 3 spin-orbit doublets. In this study, the peaks of Ti2p$_{3/2}$ and Ti2p$_{1/2}$ at 458.15 eV and 464.15 eV, respectively, are associated with the presence of TiO$_2$; the components at around 455.16 eV and 460.76 eV, respectively, are related to Ti-N bonds. Besides these chemical states, the intermediated state was found in the coating, which corresponds to Ti-N-O bonds at 456.60 eV for Ti2p$_{3/2}$ peak and 462.44 eV for Ti2p$_{1/2}$ peak, which is in good agreement with binding energy reported in the literature [87,88].

The Nb3d spectrum was fitted into 3 spine-orbit doublets. The spin-orbit split 3d$_{3/2}$ and 3d$_{5/2}$ peaks at around 206.97 eV and 203.74 eV, respectively, are correspond to the binding energy of NbN. The components at around 206.52 eV (Nb3d$_{3/2}$) and 209.46 eV (Nb3d$_{3/2}$) can be assigned to Nb$_2$O$_3$, and at 204.79 eV (Nb3d$_{5/2}$) and at 207.64 eV (Nb3d$_{3/2}$) – to NbO [89,90].

The Mo3d$_{3/2}$ and Mo 3d$_{5/2}$ peaks of the Mo3d spectrum have been de-convoluted into 3 chemical states: molybdenum nitride, MoO$_2$ and MoO$_3$ with binding energies of 228.19 eV (Mo3d$_{3/2}$) and 231.41 eV (Mo3d$_{5/2}$), 229.31 eV (Mo3d$_{3/2}$) and 231.34 eV (Mo3d$_{5/2}$), 232.69 eV (Mo3d$_{3/2}$) and 235.19 eV (Mo3d$_{5/2}$), respectively [91].

Fig. 2 shows typical depth profile of (TiZrNbTaHf)N/MoN coatings. It is clearly visible that the signal from all elements are well distinguished. The intensity can be related to a semi-quantitative concentration of the ion fragments of constituent elements along the coating thickness. Analysis of these results confirms the presence of secondary ion current oscillation, which corresponds to formation of multi-layered structure consisting of (TiZrNbTaHf)N and Mo$_2$N layers. The decreasing of intensity of the oscillations with an increasing of sputter time is not due to the destruction of a multilayer structure. In our opinion, this kind of changes could be explained by changes in sputtering rate and increasing of the curvature of the layers.

In case of GDMS analysis (see Fig. 3) it was shown, that the ion current intensities of constituent elements decreases with the increasing of thickness of each samples (see Fig. 3). This effect is due to the developing conditions of the glow discharge during the analysis. It is worth to note that nitrogen and tantalum signals are burdened by high background levels. In fact, N ion signal (measured as N$_2$H$^+$ ion current) is high due to high nitrogen background in the glow discharge cell and Ta signal is high due to the use of tantalum diaphragm as an intermediate cathode in the glow discharge cell. Nevertheless, the distribution of all the remaining elements is close to uniform, except Hf, which signal is close to the noise level.

3.2. Structural analysis and microstructure

Diffraction patterns from (TiZrNbTaHf)N/(MoN) multilayer nanocomposite coatings deposited on steel under different substrate bias are presented in Fig. 4. As we can see, XRD patterns contain FCC γ-Mo$_2$N (111), (200), (220) and (311) together with (TiZrNbTaHf)N (111), (200), (220), (222) and (311) peaks.

In Table 2, the calculated lattice constants for TiN, ZrN, HfN and TaN in a comparison with the corresponding experimental and theoretical values are showed. One can see that the calculated lattice parameters are in good agreement with those gained in experimental and theoretical investigations of other authors. Nevertheless, there is a strong deviation of the calculated values from the experimental ones for TaN, which could be ascribed to nonstoichiometry of the experimental TaN samples.

From these XRD patterns, we can observe the changing of preferred orientation from (111) + (311) to (200) under different substrate bias. At low U_s, the highest peaks are at 2θ = 69.67°, 2θ = 34.65°, which correspond the (311) and (111) planes of the (TiZrNbTaHf)N layer and 2θ = 36.11° responsible for (111) plane of the γ-Mo$_2$N layer. When substrate bias increases to −200 V, the intensity of (111) planes of
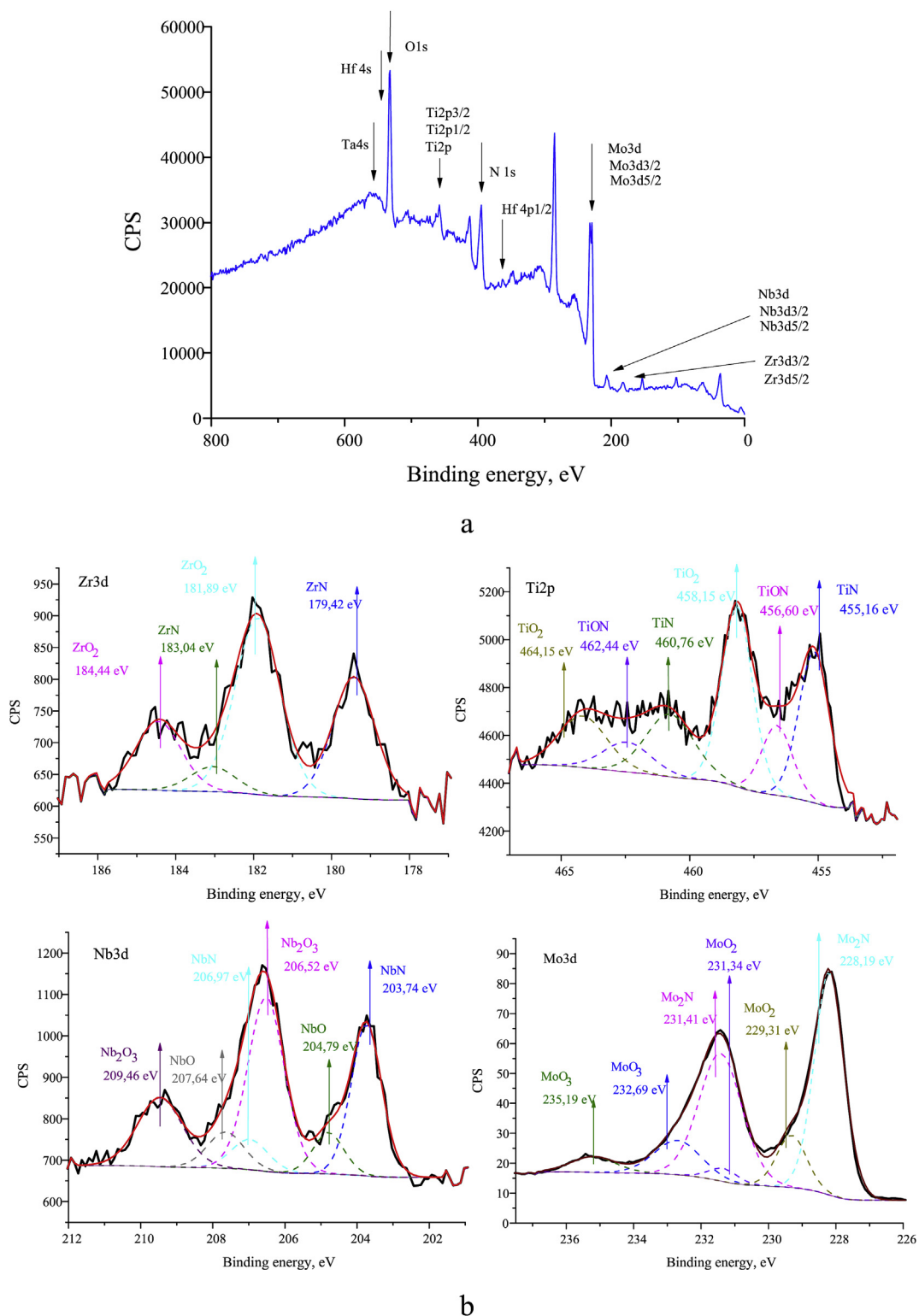
Fig. 1. XPS spectra of (TiZrNbTaHf)N/MoN coating deposited at U_{sb} = −200 V: a) XPS survey spectrum; b) Zr3d, Ti2p, Nb3d, Mo3d.

(TiZrNbTaHf)N and γ-Mo$_2$N layers reach maximum and weak (200) (TiZrNbTaHf)N, (222) (TiZrNbTaHf)N and (311) γ-Mo$_2$N peaks can be observed. The preferred orientation of (TiZrNbTaHf)N/MoN grains was dramatically changed from (111) to (200) (TiZrNbTaHf)N, (200) γ-Mo$_2$N and (220) γ-Mo$_2$N at −300 V.

Figs. 5 and 6 present TEM cross-sectional images and SAED patterns of (TiZrNbTaHf)N/MoN multilayered coatings deposited under −100 V and −300 V, respectively. STEM analysis of the (TiZrNbTaHf)N/MoN multilayered coatings, Figs. 5 and 6 b, confirm the columnar growth with dark and bright layers. Taking into account the different sputtering coefficient of the constituent atoms and EDX mappings, the bright layers on Fig. 5 b and 6 a can be as assigned to (TiZrNbTaHf)N with thickness 15–20 nm and dark layers to Mo$_2$N with thickness of around 5 nm. From SAED patterns, which show in Fig. 5 c and 6 (the inset), the reflections (111), (200), (220), (222) and (311) corresponding to the FCC phases are clearly identified. The reflections corresponding to fcc-
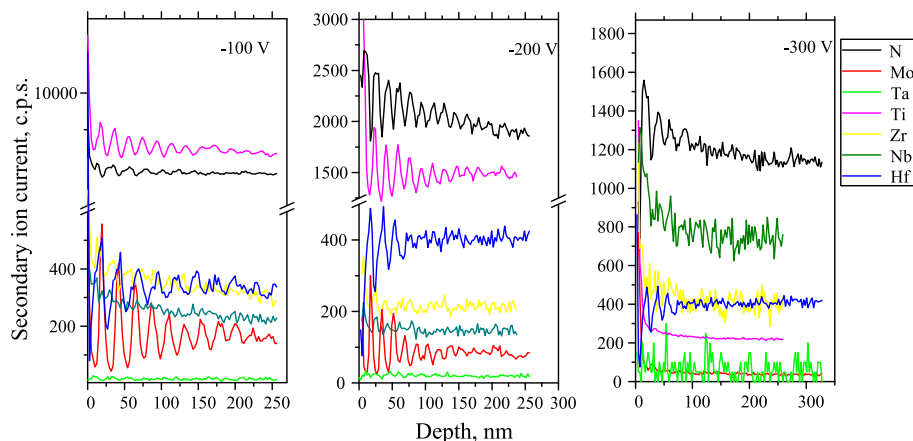
Fig. 2. SIMS analysis of N$^+$, Mo$^+$, Zr$^+$, Nb$^+$, Hf$^+$, Ti$^+$ and Ta$^+$ ion emission in time of erosion of (TiZrNbTaHf)N/MoN samples at different substrate bias. The secondary ion current data is shown in linear scale versus erosion depth.

(TiZrNbTaHf)N and fcc-Mo$_2$N phases are very close to each other, which is in good agreement with the results shown in XRD patterns. The modulation period estimated from the TEM images was 20 nm for the coating deposited at −100 V and 25 nm at −300 V. The changes in the modulation period are associated with the increase of the TiZrNbTaHf target current during deposition of the coating under −300 V.

The HRTEM images and its corresponding inverse FFT images, provide a hint of the internal structure of the columnar grains observed in the coatings (see Fig. 5 (d, e) and Fig. 6 (c, d)) demonstrating the formation of randomly oriented nanocrystalline sub-grains of (TiZrNbTaHf)N/MoN multilayered nanocomposite coatings with sizes between 5 and 15 nm (see Table 3). The inverse FFT filtering of (311) oriented grains of fcc-(TiZrNbTaHf)N and (311) oriented grains of fcc-Mo$_2$N phase of the coating deposited under −100 V (Fig. 5 e) revealed that the corresponding lattice fringes are maintained through the interface of the corresponding layers without interruption during the grain growth. Importantly, these observations imply that the grains grow "epitaxially" with fcc-(TiZrNbTaHf)N(311)||fcc-Mo$_2$N(311), or at

least, highly coherently between interfaces. This local cube on cube epitaxial growth is due to the fact that both layers have the same crystalline structure, with a lattice mismatch of around 4.6%. The same growth was observed for other orientations. Arcing of the (311)-assigned reciprocal-lattice points on the FFT pattern (Fig. 6 d, inset) points on a slight misorientation of the corresponding grains. Several arrays of mismatch dislocations were observed in HRTEM images (not showed here), which are introduced due to the relaxation of coherency strains accumulated as a result of the lattice mismatch. It should be noted, that these dislocations caused lattice distortion, which can lead to the formation of sub-grain structure.

The increase in bias voltage up to 200 V caused degradation of the (311)-oriented grains of Mo$_2$N phase, but promoted the development of (111) texture, as clearly visible on XRD pattern. Therefore, the same local epitaxy with cube on cube growth can be expected, although texturized in the (111). However, an abrupt change of the growth mechanism is observed for the coating deposited at 300 V. A complete degradation of (111) oriented MoN grains and significant sharpening of
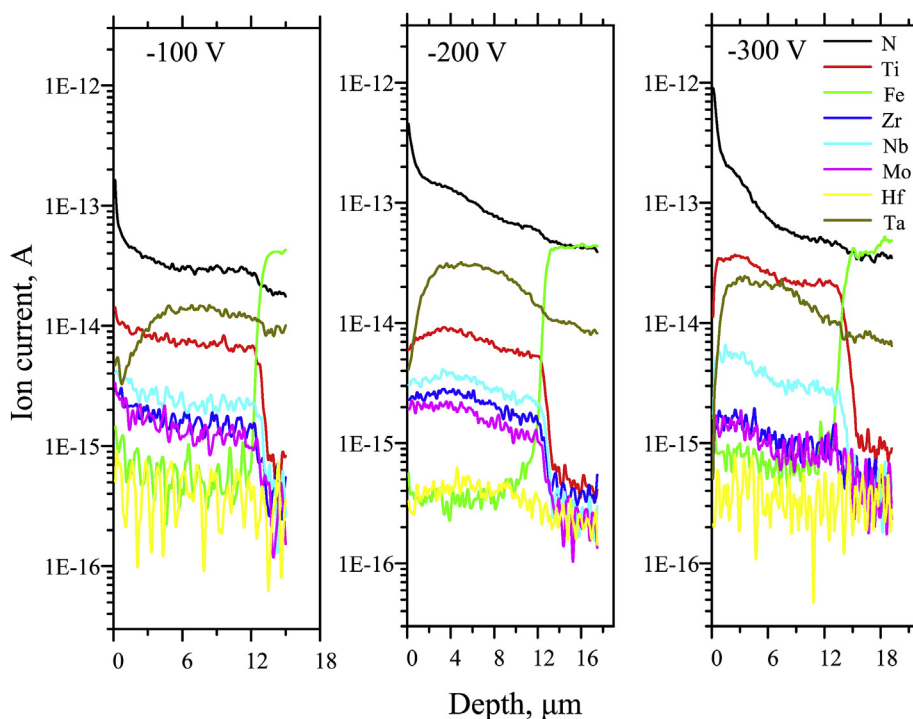

Fig. 3. GDMS analysis of (TiZrNbTaHf)N/MoN samples deposited at −100 V, −200 V and −300 V substrate bias. The ion current data is shown in logarithmic scale.
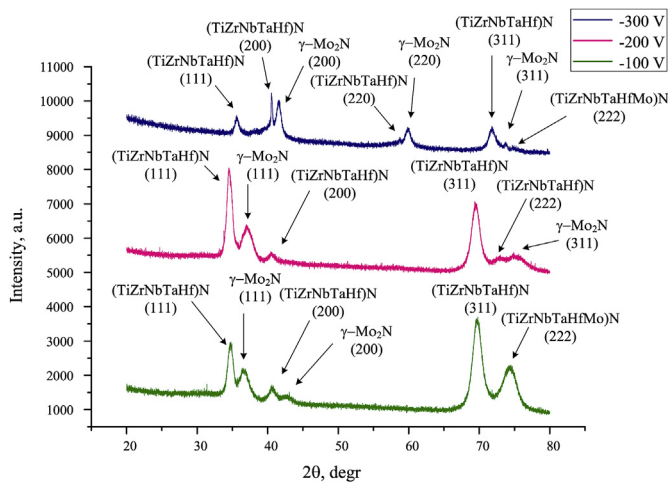
Fig. 4. XRD spectra of (TiZrNbTaHf)N/MoN multilayered nanocomposite coatings under different substrate biases.

Table 2
Calculated lattice parameters (in Å) for TiN, ZrN, HfN and TaN.

TiN	ZrN	HfN	TaN
4.247	4.592	4.537	4.407
4.241[a]	4.600[a]	4.525[a]	4.340[a]
4.25[b]	4.60[b]	4.54[b]	4.408[c]
4.275[c]	4.583[c]	4.54[c]	

[a] Experiment [92].
[b] First-principles pseudo-potential method (VASP code) + GGA [93].
[c] First-principles ultrasoft pseudo-potential method + GGA [94].

the (200) reflections of both phases, as well as a shift of other reflections of (TiZrNbTaHf)N phase to higher angles are observed. Due to much lower lattice mismatch of around 2.2%, the (200) oriented grains of both lattices demonstrated cube on cube epitaxial growth (not showed here). At the same time, the absence of (111) oriented Mo_2N grains renders impossible the coherent growth of (111) (TiZrNbTaHf)N grains with Mo_2N layer, effect that is clearly demonstrated in Fig. 6 (c, d). Importantly, there is no crystallographic coherence between the (111) (TiZrNbTaHf)N and (200) Mo_2N grains and therefore the arrays of stacking faults are introduced at the interface between the layers visible as a smearing of the reciprocal-lattice points on the FFT pattern acquired at the interfaces (Fig. 6 (e, g)).

3.3. Nano-indentation measurements

Hardness and Young's modulus values of (TiZrNbTaHf)N/MoN multilayer nanocomposite coatings are presented on Fig. 7 as a function of the indenter displacement. It is important to remark that at low penetration, roughness of the films overcomes the Berkovich shape, thus stable values can be observed above penetrations of 50 nm.

The hardness and Young's modulus strongly depend on substrate bias (see Fig. 7). The initial increase of substrate bias from −100 V to −200 leads to increase of the hardness and Young's modulus from 29 to 306 GPa to −200 V–33 and 315 GPa, respectively. At the highest substrate bias (at −300 V) the hardness and Young's modulus decreases dramatically to 20 and 349 GPa. It should be noted, that the drastic decrease of hardness of the coatings at −300 V can be explained by development of (200) preferred orientation, which is less densely packed that (111) and by increasing of grain size. Based on oscillation of the signal of constituent elements (see Fig. 3), we can conclude that the (TiZrNbTaHf)N and Mo_2N layers have sharp and distinguished interfaces. However, the increasing of substrate bias leads to large
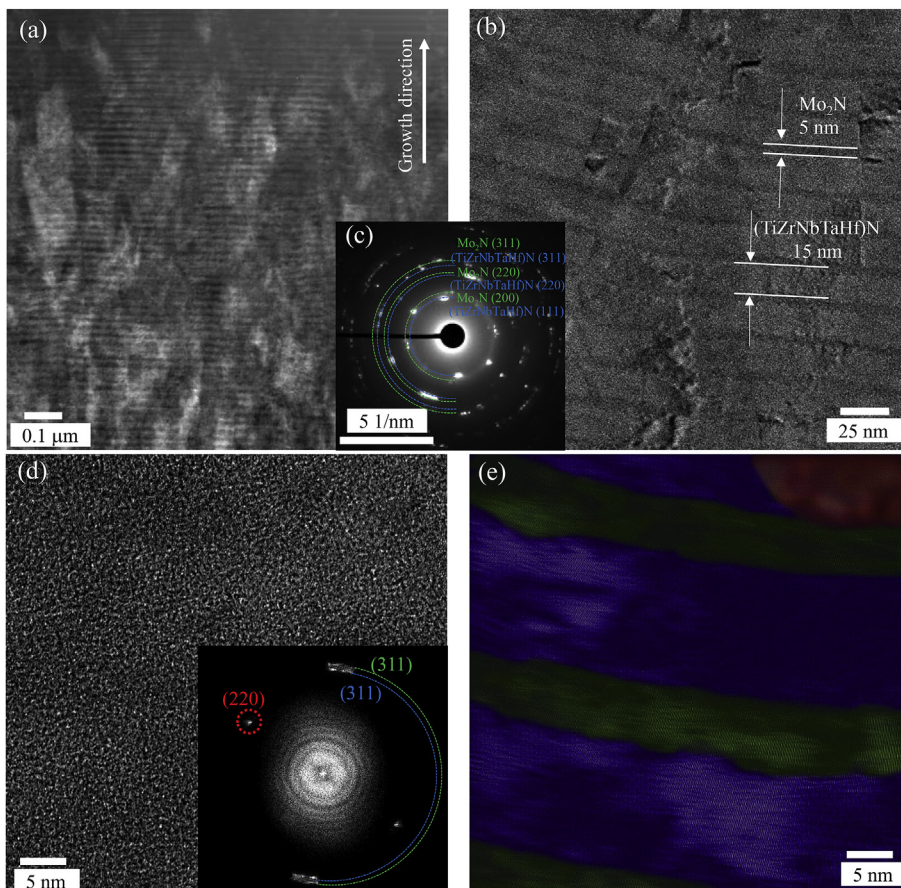

Fig. 5. Cross-sectional STEM image of the (TiZrNbTaHf)N/MoN multilayered coating obtained under −100 V (a), low-magnification bright-field TEM image (b), corresponding SAED pattern (c), high-resolution TEM image and corresponding FFT pattern as an inset (d) and inverse FFT image (e) of the image (d). The Mo_2N (311) oriented grains are colored in green color in figure e, while (TiZrNbTaHf)N grains with (311) and (220) orientations are colored in blue and red color, respectively. (For interpretation of the references to color in this figure legend, the reader is referred to the Web version of this article.)
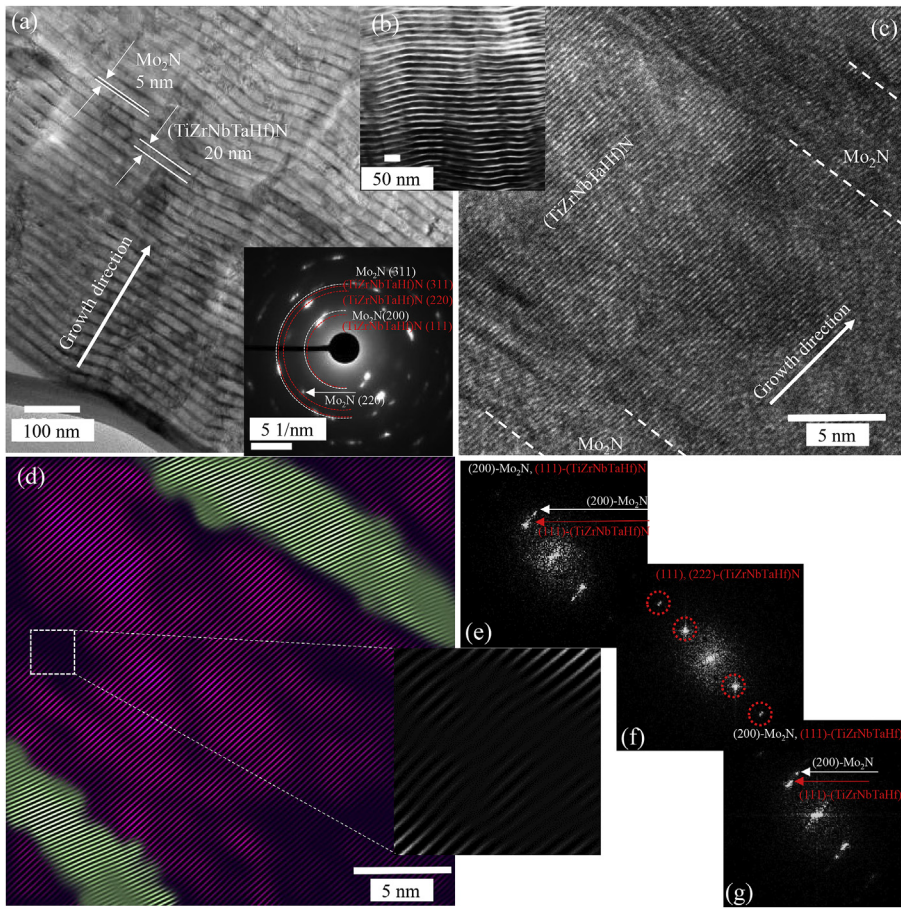
Fig. 6. Cross-sectional bright field TEM image with SAED as an inset (a), STEM image (b), and high resolution cross-sectional TEM image (c) of the (TiZrNbTaHf)N/MoN multilayered coating obtained under −300 V with corresponding inverse FFT image (d) and the local FFTs acquired from the MoN/(TiZrNbTaHf)N interface in the lower left part of figure c (b), from the (TiZrNbTaHf)N layer (e) and (TiZrNbTaHf)N/MoN interface in the upper right part of figure c (f). The Mo$_2$N (200) oriented grains are colored in green color in figure d, while (TiZrNbTaHf)N (111) oriented grains are colored in purple color. (For interpretation of the references to color in this figure legend, the reader is referred to the Web version of this article.)

Table 3
Thickness, bilayer period (Λ) and crystallite size (D) of the (TiZrNbTaHf)N/(MoN) multilayered coatings.

Substrate bias, U$_{sb}$, V	Thickness, μm	Bilayer period, Λ, nm	Crystallite size, (TiZrNbTaHf)N, D, nm	Crystallite size, (Mo$_2$N), D, nm
−100	11.5	20	9	5
−200	10	25	10	6
−300	12.2	25	15	10

diffusion of elements in the coatings, to the loss of independent interfaces and probably to incomplete layers.

Elastic strain to failure H/E* and resistance to plastic deformation H^3/E^{*2} were calculated from the nanoindentation data (Fig. 7). The best ability to resist the plastic deformation (H^3/E^{*2}) of 0.38 GPa and highest elastic strain prior to failure of 0.1 among the studied coatings demonstrates the multilayer coating deposited under −200 V substrate bias voltage.

The coefficient of thermal expansion (CTE) of the investigated nanocomposite coatings can be estimated according to the rule of mixing from the CTEs of binary nitrides of constituent elements: $\alpha_{TiN} = 8.1 \times 10^{-6}\,K^{-1}$, $\alpha_{ZrN} = 7 \times 10^{-6}\,K^{-1}$, $\alpha_{HfN} = 6.5 \times 10^{-6}\,K^{-1}$, $\alpha_{TaN} = 3.6 \times 10^{-6}\,K^{-1}$, $\alpha_{NbN} = 10.1 \times 10^{-6}\,K^{-1}$, $\alpha_{MoN} = 6.7 \times 10^{-6}\,K^{-1}$ [95–98]. As a result, the overall CTE (see Table 4) can be found from the equation [95]:

$$\alpha_{TiZrNbTaHf/MoN} = \alpha_{TiN} \times C_{TiN} + \alpha_{ZrN} \times C_{ZrN} + \alpha_{HfN} \times C_{HfN} + \alpha_{TaN} \times C_{TaN} + \alpha_{NbiN} \times C_{NbiN} + \alpha_{MoN} \times C_{MoN},$$

where C_i – is a the concentration ratio of the individual target element to the total target elements in the coating [95]. The significant difference of CTEs of (TiZrNbTaHf)N/MoN and substrate ($\alpha_{12H18N9T\ steel} - 18 \times 10^{-6}\,K^{-1}$)

could lead to evolution of larger thermal stress in the coatings. For calculation of the Young's modulus of the coatings (Table 4) by means of formula (1), we used Poisson ratio equal to $\nu = 0.25$, which is the most frequently value for nitride films reported in the literature [95,99–101].

4. Discussion

4.1. Microstructure

Our experimental analysis of chemical bonding state, elemental composition, structural-phase state and microstructure using different high-resolution methods such as SIMS, GDMS, XPS, XRD and HRTEM have shown that the (TiZrNbTaHf)N/MoN nanocomposite coatings deposited by vacuum arc deposition at different substrate bias grow with local cube on cube epitaxy of fcc-MoN and fcc-(TiZrNbTaHf)N grains. The growth of such structure can be explained by the following considerations.

Nitride coatings, like (TiZrNbTaHf)N, based on MPEAs with randomly distributed atoms tend to form a disordered solid solutions with a simple crystal structures [53–57]. It is important to note, that the crystal structure of the binary nitrides of constituent elements and their lattice parameter are approximately equal (TiN – FCC with lattice parameter, a = 0.424 nm; ZrN – FCC, a$_{ZrN}$ = 0.459 nm; NbN – FCC, a$_{NbN}$ = 0.442 nm; TaN = FCC, a$_{TaN}$ = 0.44 nm; HfN – FCC, a$_{HfN}$ = 0.453 nm) [92]. In our case the lattice parameter of (TiZrNbTaHf)N is 0.446 and 0.448 nm for the coatings deposited under −100 V and −200 V, respectively, which is close to the lattice parameter of binary nitrides of constituent elements. The N p-orbitals interact with the transition metals d-orbitals forming sp^{3}d^2 hybridization typical for the transitional metal nitrides with NaCl structure. Therefore, there is a high probability of forming NaCl structured solid-solution where the
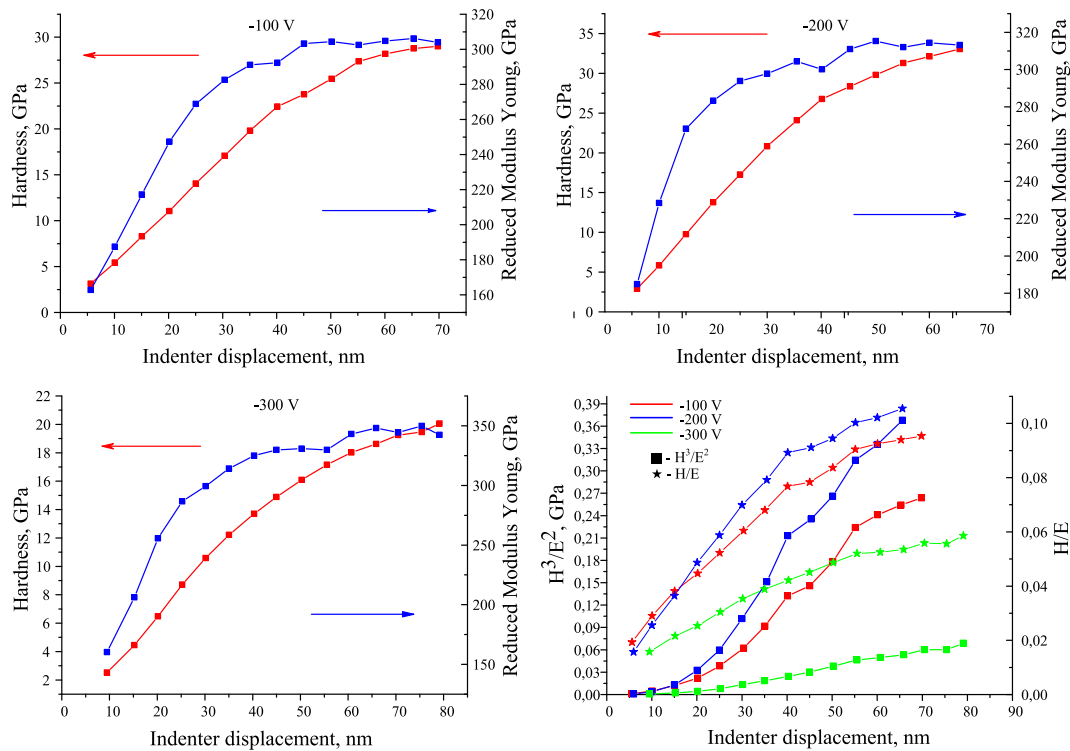
Fig. 7. Hardness, elastic modulus, H^3/E^2 and H/E ratios for (TiZrNbTaHf)N/MoN multilayered nanocomposite coatings obtained under different substrate bias.

Table 4
Poisson ratio, Young's modulus and coefficient of thermal expansion of the investigated coatings deposited under different substrate bias.

Substrate bias, V	Poisson ratio	Young's modulus, GPa	Coefficient of thermal expansion, $\times 10^{-6} \, K^{-1}$
−100	0.25	408	5.83
−200		423	6.3
−300		487	5.59

transition metals occupy the metallic sub-lattice cites.

It is well known that the metals (Ti, Zr, V, Hf, Nb, Ta, Mo, W) which belong to IV-VI groups can form binary and ternary compounds with nitrogen that are metastable disordered solid solution with FCC structure [102]. However, limited information are available on the structural phase state of multicomponent coatings. That's why we employed first-principles calculations for obtaining the general picture of phase formation in (TiZrNbTaHf)N/MoN multilayered coatings.

In our theoretical interpretation of the experimental results, we concentrate on the binary and ternary alloys. However our approach is quite justified because the goal of our theoretical study is to show the possibility of the formation of different phases in the complex (TiZrNbTaHf)N solid solutions that form the hard coatings considered above. The phase stability is based on an analysis of mixing energy. Positive mixing energy implies that a solid solution is not stable, and will decompose into separate phases with the chemical driving force (E_{mix}). Unstable alloys can be thermally stabilized in some range of compositions, because the configurational entropy is always positive and promotes a decrease in Gibbs free energy. On the contrary, a stable solid solution has negative mixing energy.

In Fig. 8, the mixing energies of the binary alloys based on titanium, zirconium, hafnium and tantalum nitrides with the B1 structure are showed. For the sake of comparison, the mixing energies calculated by a first-principles pseudo-potential method (VASP code) using the 32-atom cells with the randomized arrangement of transition metal atoms in the sites of the metallic sub-lattice [93]. For $Zr_{1-x}Ti_xN$ and $Ti_{1-x}Hf_xN$,

all non-end-member structures have positive E_{mix}. There is a little asymmetry of $E_{mix}(x)$ leaning to TiN-side in $Zr_{1-x}Ti_xN$ but much more in $Ti_{1-x}Hf_xN$ in agreement with the results [93]. Our E_{mix} values are slightly higher compared to those calculated in Ref. [93], which is supposed to be due to the ordered cells used in our calculations. The positive mixing energies are observed in $Ti_{1-x}Ta_xN$, $Zr_{1-x}Ta_xN$ and $Hf_{1-x}Ta_xN$, indicating that these alloys can be stable in a wide range of temperatures. The minimums of $E_{mix}(x)$ is located closer to TaN-side, especially in $Zr_{1-x}Ta_xN$. In our previous work [63], we have shown that the most values of mixing energy for $Ti_{1-x}Nb_xN$ in the range of $0.25 \le x \le 1$ are negative, which indicates that such alloys can be stabilized as solid solutions at moderate temperatures.

Table 4 shows the calculated mixing energy for the ternary $Zr_{1-x}Ti_yTa_{1-x-y}$, $Zr_{1-x}Hf_yTa_{1-x-y}$ and $Ti_{1-x}Hf_yTa_{1-x-y}$ alloys. The results presented in Table 5 enable us to estimate an effect of the substitutional atoms on the stability of the binary alloys considered above. The comparison of the results presented in Fig. 8 and Table 4 shows that:

1) $Zr_{1-x}Ti_xN$ and $Ti_{1-x}Hf_xN$ can be stabilized by the substitution up to 50% of Zr, Ti, Hf atoms by Ta atoms;
2) The substitution up to 50% of Ti, Hf and Ta atoms by Zr atoms in $Ti_{1-x}Ta_xN$ and $Hf_{1-x}Ta_xN$ leads to an increase in E_{mix} of these alloys;
3) $Zr_{1-x}Ta_xN$ is destabilized due to the substitution up 50% of Zr or/and Ta atoms by Ti atoms.

An analysis of the results presented in Table 5 and in our work [63] shows that along with the transition metal mononitrides and the stable binary solid solutions shown in Fig. 8, the following ternary alloys, such as $Ti_{1-x}Hf_yTa_{1-x-y}$, $Zr_{1-x}Hf_yTa_{1-x-y}$, $Zr_{0.25}Ti_{0.25}Ta_{0.5}$, $Ti_{1-x}Nb_xN$ can form in the (TiZrNbTaHf)N disordered solid solutions. It follows that the metallic matrix of the deposited nanocomposite coatings can contains transition metal mononitrides and their solid solutions, depending on deposition conditions. Due to the low mixing energy of the mentioned ternary alloys, the decomposition of corresponding solid solution phases can take at a relatively high temperature, thus will be responsible for the stability of the coating system at high thermal loads.
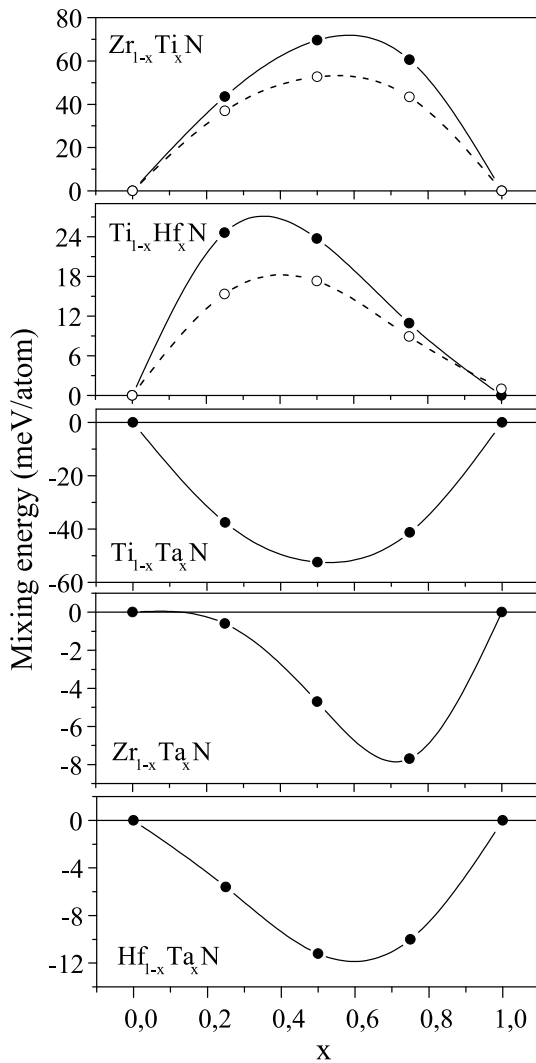
Fig. 8. Calculated mixing energies (full circles) for Me1$_{1-x}$Me2$_x$N alloys (Me1, Me2 = Ti, Zr, Hf, Ta) as functions of composition x. Open circles are the results reported in Ref. [92]. Solid and dashed lines are the spline approximation of the calculated points.

Table 5
Mixing energy (E$_{mix}$) for the ternary alloys.

Solid solution	E$_{mix}$ (meV/ atom)	Solid solution	E$_{mix}$ (meV/ atom)	Solid solution	E$_{mix}$ (meV/ atom)
Zr$_{0.25}$Ti$_{0.25}$Ta$_{0.5}$	−10.9	Zr$_{0.25}$Hf$_{0.25}$Ta$_{0.5}$	−7.8	Ti$_{0.25}$Hf$_{0.25}$Ta$_{0.5}$	−25.1
Zr$_{0.25}$Ti$_{0.5}$Ta$_{0.25}$	13.1	Zr$_{0.25}$Hf$_{0.5}$Ta$_{0.25}$	−3.6	Ti$_{0.25}$Hf$_{0.5}$Ta$_{0.25}$	−4.8
Zr$_{0.5}$Ti$_{0.25}$Ta$_{0.25}$	20.5	Zr$_{0.5}$Hf$_{0.25}$Ta$_{0.25}$	−1.9	Ti$_{0.5}$Hf$_{0.25}$Ta$_{0.25}$	−11.7

It is worth to note that Mo is a weaker nitride-forming element characterized by low enthalpy of formation $\Delta H^{Mo2N} = -81.6$ kJ/mol in contrast with strong nitride-forming elements, like Ti, Ta, Zr and Nb, with easy nucleation: $\Delta H^{TiN} = -335$ kJ/mol, $\Delta H^{TaN} = -252$ kJ/mol, $\Delta H^{ZrN} = -365$ kJ/mol, $\Delta H^{NbN} = -234.7$ kJ/mol, $\Delta H^{HfN} = -373.6$ kJ/mol. Nevertheless, the obtaining of solid solution with simple structure in (Ti-Zr-Nb-Hf-Ta)N/MoN coatings can be anticipated based on the aforementioned fact.

Thus, according to Hume-Rothery rules [103], the formation of the solid solutions is very favourable as a consequence of the relatively low atomic size mismatch between the constituent atoms, the small electronegativity difference and the small valence difference between Nb,

Ta, Hf, Zr and Ti in addition to the mentioned above a low energy difference between the corresponding nitride phases. Indeed, the diffraction peak positions associated with (TiZrNbTaHf)N phase of the coatings deposited under −100 V and −200 V are in the intermediate position between stress-free TiN and HfN. This can be assigned to NaCl lattice dilatation due to random occupation of the metal sub-lattice sites by bigger atoms than Ti ($r_{Ti} = 1.40$ Å) such as Hf ($r_{Hf} = 1.55$ Å), Ta ($r_{Ta} = 1.45$ Å), Zr ($r_{Zr} = 1.55$ Å) and Nb ($r_{Nb} = 1.45$ Å).

MoN layers from investigated samples are polycrystalline exhibiting diffraction peaks related to cubic γ-Mo$_2$N phase. Recently, I. Jauberteau et al. [104]. have reported that there are three molybdenum nitride phases which are stable in thermal equilibrium (γ-Mo$_2$N with cubic structure of NaCl B1-type, β-Mo$_2$N – tetragonal modification of γ-Mo$_2$N phase and δ-Mo$_2$N – hexagonal structure). Molybdenum nitride also can be synthesized in the thermodynamically unstable stoichiometric MoN phase of NaCl-B1-type cubic structure. The formation of such phase place demands high temperature and concentration of nitrogen. It should be noted that, it is difficult to determine the kind of phases of MoN from XRD studies. Especially it related to γ-Mo$_2$N and β-Mo$_2$N phases, which have a similar intense of reflection at low Bragg angles [4,105]. In our case, the lattice parameter of 0.416–0.418 nm of MoN (obtained from XRD peak positions) is close to the values obtained by *Bull* et al. [106], *Ihara* et al. [107], *Stöber* et al. [108], which correspond γ-Mo$_2$N phase of Fm3m space group.

It was shown that the application of different substrate biases leads to microstructural modification in terms of the films preferred crystal orientation. At low U$_s$ a strong (111) and (311) peaks of (TiZrNbTaHf)N and (111) of Mo$_2$N was found. Under higher energetic conditions (at −300 V) more closed packed (111) plane reduced and eventually disappeared (in the case of Mo$_2$N) and there is an evolution of more open channeling planes: (200) of (TiZrNbTaHf)N and (200), (220) of Mo$_2$N. Such textural changes are known due to the competition between thermodynamic and kinetic forces: enhanced ad-atom mobility, plasma sheath, re-sputtering yield, anisotropy in surface diffusivities, cascade effects, free surface and strain energies.

It should be noted, that the more intensive (311) orientation, which is parallel to the sample surface. In contrast, the (111) orientation can attributed to the difference in growth rates between the two crystallographic planes and by a preferential re-sputtering of the N atoms lying on the (111) planes under high ion bombardment deposition at −300 V [109,110]. Moreover, the clearly visible XRD peak-shift of the (TiZrNbTaHf)N reflections toward higher angle positions for the coating deposited under −300 V substrate bias is a consequence of the lattice shrinking. This is a result of the depletion of the plasma flow on big atoms that is well demonstrated by EDS analysis (Table 6). As a possible explanation of this depletion one can consider the increase of the target current during the deposition of the coating deposited under 300 V. The increase of the target current from 90 A to 120 A, give rise to the increment of the target temperature, thus increasing its poisoning by N. The formation of the nitrides of the constituting elements on the target results in the preferential erosion of more easily eroded phases like TiN (T$_m$ = 2949 °C), ZrN (T$_m$ = 2980 °C) and NbN (T$_m$ = 2573 °C) compared to HfN (T$_m$ = 3310 °C) and TaN (T$_m$ = 3090 °C) whose depletion is observed. This preferential erosion may subsequently influence the composition evolution of the plasma and the resultant film

Table 6
EDS quantification of metallic elements for the (TiZrNbTaHf)N/MoN coatings deposited at −100 V, −200 V and −300 V substrate bias. ("–"means that the element was not quantified due to its low concentration).

U$_{sb}$	Ti	Zr	Nb	Hf	Ta	Mo
100	16.07	12.10	5.34	12.16	10.91	43.41
200	15.66	11.44	10.35	6.39	6.03	50.13
300	43.23	13.01	19.45	–	0.08	24.23

composition visible as enrichment on Ti and Nb.

Recently, many works have shown the influence of substrate bias on the orientation of growth plane, like the transition from (111) to (200) preferred orientation in different nitride systems: Cr-Mo-N [111], Ti-Al-N [112], CrN/AlBN [113], TiAlLaN [114], TiN-MoS$_x$ [115], TiAlSiN [116], (Al$_{1.5}$CrNb$_{0.5}$Si$_{0.5}$Ti)N$_x$ [117] and others [55,118,119]. However, the detailed physical mechanism of the development of preferred orientation under the influence of substrate bias is not yet fully understood.

The textural evolution of (TiZrNbTaHf)N/MoN multilayered nanocomposite coatings can be described through a complex of interplay between thermodynamic and kinetic forces, which have been recently studied for TiN [120–125]. From the point of view of modern thermodynamics, minimal total energy, which consist of surface, stopping and strain energy responsible for evolution of (200), (220) and (111) planes, respectively. According to this mechanism, the (111) crystallographic orientation is more favorable in the case of low ion-bombarding-energy conditions; this is due to the occupation of lower-energy position by the adatoms. In this case, the probability of growth of the (111) already nucleated grain is higher than the probability of nucleation of a new grain. Moreover, the higher Ti adatom mobility on (200) compared to (111) surface, for which Ti adatom chemical potential is $\mu_{Ti,111} < \mu_{Ti,200}$, promotes Ti adatoms moving off the (200) islands and to their adjacent (111) grains. Thus, with increasing bias voltage the collision, and therefore the mobility of adatoms also increases, consequently the deposition conditions closely approach the thermodynamic equilibrium, which leads to prevailing of thermodynamic forces under kinetic regimes. Therefore, the development of planes with minimum surface energy during nucleation and coalescence stages, which is preferred to less compact (200) orientation, is observed under high ion irradiation conditions. Additionally, the increase of adatom mobility at 300 V increases the probability of (200) islands to expand laterally.

However, there are some works [126–129], which suggest that the model, which we have described above, is doubtful. Recently, different mechanism of growth process (anisotropy in surface diffusivities, collisional cascade effects and adatom mobility's) based on kinetic driving force was proposed [121,128,129]. The high-energy condition of deposition at −300 V leads to development and evolution of more open channel directions (e.g. 200, 220) due to the larger penetration depth of incident ions (collision cascade effects). The higher energy of ions leads to the increasing of density of defects, and as a result the most close packed plane (111) in FCC crystal structure become more affected by different type of cascades.

4.2. Mechanical properties

The main mechanism responsible for the hardening of the (TiZrNbTaHf)N layer is solid-solution strengthening due to impeding dislocation motion at local stress fields created by the solute atoms. The solid-solution hardening in the coating deposited at 300 V has lower contribution to the hardening because of lower amount of solute elements in the lattice.

Multilayer architecture allows to achieve higher hardness comparing with monolithic coatings due to the impeding dislocation motion across the interfaces and due to the difference in elastic modulus of the layers. Moreover, the enhancement of hardness is due to the reduction of grain size (Hall-Petch strengthening), which is a result of the increasing of volume fraction of grain boundaries with high interfacial energies [130]. The formation of strong MeN chemical bonds and low modulation period (5–20 nm) also a reason for the enhancements of hardness. In our case, the highest hardness 29 GPa has the coating with the thinnest bilayer period (20 nm).

The high H/E*ratio imply that a typical tribo-contact during sliding/abrasive wear can remain elastic and recover due to the increased ability of the coating material to absorb energy during deformation up

to fracture at high stresses. Therefore wear resistance of the coating with H/E × ratio in the range of 0.1 [131] can be improved at high loads due to absence of plastic deformation. The high H^3/E^2 ratio means that the coating possess higher fracture toughness among the studied coatings suggesting that the resistance of the coating to the cracking sufficiently high and contributes to the protective efficiency of the coating exposed to the external load [132].

5. Conclusions

1. The deposited (TiZrNbTaHf)N/MoN multilayered nanocomposite coatings obtained by vacuum-arc deposition under different energy conditions have a complex chemical composition, which consists of nitrides of constituent elements. The presence of contaminations H$^+$, C$^+$, Na$^+$, K$^+$ and Cr$^+$ ions from ambient atmosphere was found in the coatings.

2. The formation of (TiZrNbTaHf)N and Mo$_2$N phases with FCC crystal structure was revealed in all coatings. The change of preferred orientation from (111) & (311) to less packed (200) under conditions of high substrate bias was observed. Using first-principles calculations it was shown that the metallic matrix of the (TiZrNbTaHf)N coatings can contain transition metal mononitrides and their solid solutions, depending on deposition conditions.

3. The HR-TEM observations revealed that the coatings have columnar growth and consist of multilayers with modulation period between 20 and 25 nm. The sub-grain structure of the columnar grains is composed of nanodimentional grains, which grow with local cube on cube epitaxy with coherent interfaces. The elemental inter-diffusion process between intrinsic layers was identified by EDS line scan.

4. The maximum hardness of approximately 29 GPa was obtained at a bias voltage of −200 V and the thinnest modulation period of bilayer (20 nm). The enhancement of mechanical properties was attributed to Hall-Petch strengthening, solid-solution strengthening, formation of strong MeN chemical bonds and low modulation period. Good ability to resist the plastic deformation (H^3/E^2 ratio) allows to use (TiZrNbTaHf)N/MoN multilayered nanocomposite coatings as a protective materials.

Authors contributions

A.A.B: Manuscript preparation, Sample preparation, analyzed and conducted general organization of results. **A.V.P:** Manuscript preparation, Analyzed XPS, Nanoindentation, HR-TEM, Performed FIB cross sections **L.E.C:** Manuscript preparation, experiments and analysis of XRD, Nanoindentation and HR-TEM, **P. K. & M. M**: SIMS and GDMS experiments, **V.I.I & N.R.M**: Simulations and modeling, **M.K:** XPS experiments, **V.M.B:** Samples deposition and fine tunning, **A.D.P & S.J:** Project supervision & Analysis of results.

Acknowledgement

Appendix A. Supplementary data

Supplementary data related to this article can be found at http://dx.doi.org/10.1016/j.compositesb.2018.04.015.

References

[1] Cavaleiro A, De Hosson JTM. Nanostructured coatings. New York: Springer-Verlag; 2006.

[2] Yousaf MI, Pelenovich VO, Yang B, Liu CS, Fu DJ. Influence of substrate rotation speed on the structure and mechanical properties of nanocrystalline AlTiN/Mon coatings synthesized by cathodic arc ion-plating. Surf Coating Technol 2015;265:117–24. http://dx.doi.org/10.1016/j.surfcoat.2015.01.049.

[3] Kawata K, Sugimura H, Takai O. Characterization of multilayer films of Ti-Al-O-C-N system prepared by pulsed d.c. plasma-enhanced chemical vapor deposition. Thin Solid Films 2001;390:64–9. http://dx.doi.org/10.1016/S0040-6090(01)00939-7.

[4] Pogrebnjak AD, Eyidi D, Abadias G, Bondar OV, Beresnev VM, Sobol OV. Structure and properties of arc evaporated nanoscale TiN/Mon multilayered systems. Int J Refract Met Hard Mater 2015;48:222–8. http://dx.doi.org/10.1016/j.ijrmhm.2014.07.043.

[5] Yamamoto K, Kujime S, Takahara K. Properties of nano-multilayered hard coatings deposited by a new hybrid coating process: combined cathodic arc and unbalanced magnetron sputtering. Surf Coating Technol 2005;200:435–9. http://dx.doi.org/10.1016/j.surfcoat.2005.02.175.

[6] Tian CX, Yang B, Yan SJ, Lu ZH, Huang ZH, Fu DJ. Influence of substrate rotation speed on the structure and mechanical properties of AlTiN/CrN coatings. Surf Coating Technol 2013;228:S228–32. http://dx.doi.org/10.1016/j.surfcoat.2012.05.141.

[7] Yousaf MI, Pelenovich VO, Yang B, Liu CS, Fu DJ. Effect of bilayer period on structural and mechanical properties of nanocomposite TiAlN/Mon multilayer films synthesized by cathodic arc ion-plating. Surf Coating Technol 2015;282:94–102. http://dx.doi.org/10.1016/j.surfcoat.2015.10.018.

[8] Kumar DD, Kumar N, Kalaiselvam S, Dash S, Jayavel R. Wear resistant super-hard multilayer transition metal-nitride coatings. Surfaces and Interfaces 2017;7:74–82. http://dx.doi.org/10.1016/j.surfin.2017.03.001.

[9] Chang Y-Y, Chiu W-T, Hung J-P. Mechanical properties and high temperature oxidation of CrAlSiN/TiVN hard coatings synthesized by cathodic arc evaporation. Surf Coating Technol 2016;303:18–24. http://dx.doi.org/10.1016/j.surfcoat.2016.02.047.

[10] Pogrebnjak AD, Bagdasaryan AA, Pshyk A, Dyadyura K. Adaptive multicomponent nanocomposite coatings in surface engineering. Phys Usp 2017;60 586–607. doi:10.3367/UFNe.2016.12.038018.

[11] Iatsunskyi I, Coy E, Viter R, Nowaczyk G, Jancelewicz M, Baleviciute I, et al. Study on structural, mechanical, and optical properties of Al_2O_3–TiO_2 nanolaminates prepared by atomic layer deposition. J Phys Chem C 2015;119:20591–9. http://dx.doi.org/10.1021/acs.jpcc.5b06745.

[12] Baitimirova M, Viter R, Andzane J, Van Der Lee A, Voiry D, Iatsunskyi I, et al. Tuning of structural and optical properties of graphene/ZnO nanolaminates. J Phys Chem C 2016;120:23716–25. http://dx.doi.org/10.1021/acs.jpcc.6b07221.

[13] Coy E, Yate L, Kabacińska Z, Jancelewicz M, Jurga S, Iatsunskyi I. Topographic reconstruction and mechanical analysis of atomic layer deposited Al_2O_3/TiO_2 nanolaminates by nanoindentation. Mater Des 2016;111:584–91. http://dx.doi.org/10.1016/j.matdes.2016.09.030.

[14] Coy E, Yate L, Valencia DP, Aperador W, Siuzdak K, Torruella P, et al. High electrocatalytic response of a mechanically enhanced NbC nanocomposite electrode toward hydrogen evolution reaction. ACS Appl Mater Interfaces 2017;9:30872–9. http://dx.doi.org/10.1021/acsami.7b10317.

[15] Shypylenko A, Pshyk AV, Grześkowiak B, Medjanik K, Peplinska B, Oyoshi K, et al. Effect of ion implantation on the physical and mechanical properties of Ti-Si-N multifunctional coatings for biomedical applications. Mater Des 2016:110. http://dx.doi.org/10.1016/j.matdes.2016.08.050.

[16] Vladescu A, Kiss A, Popescu A, Braic M, Balaceanu M, Braic V, Tudor I, Logofatu C, Negrila CCRR. Influence of bilayer period on the characteristics of nanometre-scale ZrN/TiAlN multilayers. J Nanosci Nanotechnol 2008;8:717–21. http://dx.doi.org/10.1166/jnn.2008.D218.

[17] Braic M, Balaceanu M, Braic V, Vladescu a, Pavelescu G, Albulescu M. Synthesis and characterization of TiN, TiAlN and TiN/TiAlN biocompatible coatings. Surf Coating Technol 2005;200:1014–7. http://dx.doi.org/10.1016/j.surfcoat.2005.02.140.

[18] Shinn M, Hultman L, Barnett SA. Growth, structure, and microhardness of epitaxial TiN/NbN superlattices. J Mater Res 1992:7.

[19] Xu J, Kamiko M, Zhou Y, Yamamoto R, Li G, Gu M. Superhardness effects of heterostructure NbN/TaN nanostructured multilayers. J Appl Phys 2001;89:3674–8. http://dx.doi.org/10.1063/1.1353809.

[20] Alizada AN, Sofiyev AH. On the mechanics of deformation and stability of the beam with a nanocoating. J Reinforc Plast Compos 2011;30:1583–95. http://dx.doi.org/10.1177/0731684411428382.

[21] Söderberg H, Odén M, Molina-Aldareguia JM, Hultman L. Nanostructure formation during deposition of TiN/SiNx nanomultilayer films by reactive dual magnetron sputtering. J Appl Phys 2005;97. http://dx.doi.org/10.1063/1.1935135. 114327–1–114327–8.

[22] Zhang GP, Liu Y, Wang W, Tan J. Experimental evidence of plastic deformation instability in nanoscale Au/Cu multilayers. Appl Phys Lett 2006;88. http://dx.doi.org/10.1063/1.2159581. 13105–1–013105–3.

[23] Toda-Caraballo I. A general formulation for solid solution hardening effect in multicomponent alloys. Scripta Mater 2017;127:113–7. http://dx.doi.org/10.1016/j.scriptamat.2016.09.009.

[24] Pogrebnjak AD, Bagdasaryan AA, Yakushchenko IV, Beresnev VM. The structure and properties of high-entropy alloys and nitride coatings based on them. Russ

Chem Rev 2014;83:1027–61. http://dx.doi.org/10.1070/RCR4407.

[25] Miracle DB, Senkov ON. A critical review of high entropy alloys and related concepts. Acta Mater 2017;122:448–511. http://dx.doi.org/10.1016/j.actamat.2016.08.081.

[26] Zhang Y, Zuo TT, Tang Z, Gao MC, Dahmen KA, Liaw PK, et al. Microstructures and properties of high-entropy alloys. Prog Mater Sci 2014;61:1–93. http://dx.doi.org/10.1016/j.pmatsci.2013.10.001.

[27] Yeh JW, Chen SK, Lin SJ, Gan JY, Chin TS, Shun TT, et al. Nanostructured high-entropy alloys with multiple principal elements: novel alloy design concepts and outcomes. Adv Eng Mater 2004;6. http://dx.doi.org/10.1002/adem.200300567. 299–303 + 274.

[28] Ye YF, Wang Q, Lu J, Liu CT, Yang Y. High-entropy alloy: challenges and prospects. Mater Today 2016;19:349–62. http://dx.doi.org/10.1016/j.mattod.2015.11.026.

[29] Yeh JW, Chen YL, Lin SJ, Chen SK. High-entropy alloys – a new era of exploitation. Mater Sci Forum 2007;560:1–9. doi:10.4028 www.scientific.net/MSF.560.1.

[30] Cantor B, Chang ITH, Knight P, Vincent AJB. Microstructural development in equiatomic multicomponent alloys. Mater Sci Eng, A 2004;375–377:213–8. http://dx.doi.org/10.1016/j.msea.2003.10.257.

[31] Takeuchi A, Chen N, Wada T, Yokoyama Y, Kato H, Inoue A, et al. Pd20Pt20Cu20Ni20P20 high-entropy alloy as a bulk metallic glass in the centimeter. Intermetallics 2011;19:1546–54. http://dx.doi.org/10.1016/j.intermet.2011.05.030.

[32] Vaidya M, Armugam S, Kashyap S, Murty BS. Amorphization in equiatomic high entropy alloys. J Non-Cryst Solids 2015;413:8–14. http://dx.doi.org/10.1016/j.jnoncrysol.2015.01.015.

[33] Gao XQ, Zhao K, Ke HB, Ding DW, Wang WH, Bai HY. High mixing entropy bulk metallic glasses. J Non-Cryst Solids 2011;357:3557–60. http://dx.doi.org/10.1016/j.jnoncrysol.2011.07.016.

[34] Xian X, Zhong Z, Zhang B, Song K, Chen C, Wang S, et al. A high-entropy V35Ti35Fe15Cr10Zr5 alloy with excellent high-temperature strength. Mater Des 2017;121:229–36. http://dx.doi.org/10.1016/j.matdes.2017.02.029.

[35] Li J, Craeghs W, Jing C, Gong S, Shan F. Microstructure and physical performance of laser-induction nanocrystals modified high-entropy alloy composites on titanium alloy. Mater Des 2017;117:363–70. http://dx.doi.org/10.1016/j.matdes.2016.12.007.

[36] Vorobiov SI, Kondrakhova DM, Nepijko SA, Pod4remne DV, Shumakova NI, Protsenko IY. Crystalline structure, electrophysical and magnetoresistive properties of high entropy film alloys. J Nano- Electron Phys 2016;8:1–5. http://dx.doi.org/10.21272/jnep.8(3).03026.

[37] Koželj P, Vrtnik S, Jelen A, Jazbec S, Jagličić Z, Maiti S, et al. Discovery of a superconducting high-entropy alloy. Phys Rev Lett 2014;113:1–5. http://dx.doi.org/10.1103/PhysRevLett.113.107001.

[38] Zhang Y, Zuo T, Cheng Y, Liaw PK. High-entropy alloys with high saturation magnetization, electrical resistivity, and malleability. Sci Rep 2013;3:1–7. http://dx.doi.org/10.1038/srep01455.

[39] Kao YF, Chen SK, Chen TJ, Chu PC, Yeh JW, Lin SJ. Electrical, magnetic, and Hall properties of AlxCoCrFeNi high-entropy alloys. J Alloy Comp 2011;509:1607–14. http://dx.doi.org/10.1016/j.jallcom.2010.10.210.

[40] Li P, Wang A, Liu CT. A ductile high entropy alloy with attractive magnetic properties. J Alloy Comp 2017;694:55–60. http://dx.doi.org/10.1016/j.jallcom.2016.09.186.

[41] Hongbao C, Ying W, Jinyong W, Xuefeng G, Hengzhi F. Microstructural evolution and corrosion behavior of directionally solidified FeCoNiCrAl high entropy alloy. China Foundry 2011;8:259–63.

[42] Lee CP, Chen YY, Hsu CY, Yeh JW, Shih HC. The effect of boron on the corrosion resistance of the high entropy alloys Al[sub 0.5]CoCrCuFeNiB[sub x]. J Electrochem Soc 2007;154. http://dx.doi.org/10.1149/1.2744133. C424.

[43] Yate L, Coy LE, Aperador W. Robust tribo-mechanical and hot corrosion resistance of ultra-refractory Ta-Hf-C ternary alloy films. Sci Rep 2017;7:1–9. http://dx.doi.org/10.1038/s41598-017-03181-2.

[44] Kunce I, Polanski M, Bystrzycki J. Structure and hydrogen storage properties of a high entropy ZrTiVCrFeNi alloy synthesized using Laser Engineered Net Shaping (LENS). Int J Hydrogen Energy 2013;38:12180–9. http://dx.doi.org/10.1016/j.ijhydene.2013.05.071.

[45] Kao YF, Chen SK, Sheu JH, Lin JT, Lin WE, Yeh JW, et al. Hydrogen storage properties of multi-principal-component CoFeMnTixVyZrz alloys. Int J Hydrogen Energy 2010;35:9046–59. http://dx.doi.org/10.1016/j.ijhydene.2010.06.012.

[46] Kunce I, Polanski M, Bystrzycki J. Microstructure and hydrogen storage properties of a TiZrNbMoV high entropy alloy synthesized using Laser Engineered Net Shaping (LENS). Int J Hydrogen Energy 2014;39:9904–10. http://dx.doi.org/10.1016/j.ijhydene.2014.02.067.

[47] Luo H, Li Z, Raabe D. Hydrogen enhances strength and ductility of an equiatomic high-entropy alloy. Sci Rep 2017;7:1–7. http://dx.doi.org/10.1038/s41598-017-10774-4.

[48] Kao Y-F, Hung C-I, Chang S-H, Yeh J-W, Hsu W-K. High entropy alloy mediated growth of graphene. CrystEngComm 2014;16:6187–94. http://dx.doi.org/10.1039/c4ce00227j.

[49] Li Z, Tasan CC, Pradeep KG, Raabe D. A TRIP-assisted dual-phase high-entropy alloy: grain size and phase fraction effects on deformation behavior. Acta Mater 2017;131:323–35. http://dx.doi.org/10.1016/j.actamat.2017.03.069.

[50] Li Z, Tasan CC, Springer H, Gault B, Raabe D. Interstitial atoms enable joint twinning and transformation induced plasticity in strong and ductile high-entropy alloys. Sci Rep 2017;7:1–7. http://dx.doi.org/10.1038/srep40704.

[51] Raabe D, Tasan CC, Springer H, Bausch M. From high-entropy alloys to high-entropy steels. Steel Res Int 2015;86:1127–38. http://dx.doi.org/10.1002/srin.201500133.

[52] Li Z, Pradeep KG, Deng Y, Raabe D, Tasan CC. Metastable high-entropy dual-phase alloys overcome the strength-ductility trade-off. Nature 2016;534:227–30. http://dx.doi.org/10.1038/nature17981.

[53] Pogrebnjak a D, Yakushchenko IV, Bagdasaryan a a, Bondar OV, Krause-Rehberg R, Abadias G, et al. Microstructure, physical and chemical properties of nanostructured (Ti–Hf–Zr–V–Nb)N coatings under different deposition conditions. Mater Chem Phys 2014;147:1079–91. http://dx.doi.org/10.1016/j.matchemphys.2014.06.062.

[54] Tsai M-H, Wang C-W, Lai C-H, Yeh J-W, Gan J-Y. Thermally stable amorphous (AlMoNbSiTaTiVZr)50N50 nitride film as diffusion barrier in copper metallization. Appl Phys Lett 2008;92:52109. http://dx.doi.org/10.1063/1.2841810.

[55] Tsai D-C, Liang S-C, Chang Z-C, Lin T-N, Shiao M-H, Shieu F-S. Effects of substrate bias on structure and mechanical properties of (TiVCrZrHf)N coatings. Surf Coating Technol 2012;207:293–9. http://dx.doi.org/10.1016/j.surfcoat.2012.07.004.

[56] Chang SY, Huang YC, Li CE, Hsu HF, Yeh JW, Lin SJ. Improved diffusion-resistant ability of multicomponent nitrides: from unitary TiN to senary high-entropy (TiTaCrZrAlRu)N. JOM (J Occup Med) 2013;65:1790–6. http://dx.doi.org/10.1007/s11837-013-0676-2.

[57] Chang ZC, Tsai DC, Chen EC. Structure and characteristics of reactive magnetron sputtered (CrTaTiVZr)N coatings. Mater Sci Semicond Process 2015;39:30–9. http://dx.doi.org/10.1016/j.mssp.2015.04.045.

[58] Braic V, Vladescu A, Balaceanu M, Luculescu CR, Braic M. Nanostructured multi-element (TiZrNbHfTa)N and (TiZrNbHfTa)C hard coatings. Surf Coating Technol 2012;211:117–21. http://dx.doi.org/10.1016/j.surfcoat.2011.09.033.

[59] Rost CM, Sachet E, Borman T, Moballegh A, Dickey EC, Hou D, et al. Entropy-stabilized oxides. Nat Commun 2015;6:1–8. http://dx.doi.org/10.1038/ncomms9485.

[60] Lin MI, Tsai MH, Shen WJ, Yeh JW. Evolution of structure and properties of multi-component (AlCrTaTiZr)Ox films. Thin Solid Films 2010;518:2732–7. http://dx.doi.org/10.1016/j.tsf.2009.10.142.

[61] Berardan D, Meena AK, Franger S, Herrero C, Dragoe N. Controlled Jahn-Teller distortion in (MgCoNiCuZn)O-based high entropy oxides. J Alloy Comp 2017;704:693–700. http://dx.doi.org/10.1016/j.jallcom.2017.02.070.

[62] Hsu C-Y, Yeh J-W, Chen S-K, Shun T-T. Wear resistance and high-temperature compression strength of Fcc CuCoNiCrAl0.5Fe alloy with boron addition. Metall Mater Trans A 2004;35:1465–9. http://dx.doi.org/10.1007/s11661-004-0254-x.

[63] Pogrebnjak AD, Bagdasaryan AA, Beresnev VM, Nyemchenko US, Ivashchenko VI, Kravchenko YO, et al. The effects of Cr and Si additions and deposition conditions on the structure and properties of the (Zr-Ti-Nb)N coatings. Ceram Int 2017;43:771–82. http://dx.doi.org/10.1016/j.ceramint.2016.10.008.

[64] Pogrebnjak AD, Yakushchenko IV, Bondar OV, Beresnev VM, Oyoshi K, Ivasishin OM, et al. Irradiation resistance, microstructure and mechanical properties of nanostructured (TiZrHfVNbTa)N coatings. J Alloy Comp 2016;679:155–63. http://dx.doi.org/10.1016/j.jallcom.2016.04.064.

[65] Yu R-S, Huang R-H, Lee C-M, Shieu F-S. Synthesis and characterization of multi-element oxynitride semiconductor film prepared by reactive sputtering deposition. Appl Surf Sci 2012;263:58–61. http://dx.doi.org/10.1016/j.apsusc.2012.08.109.

[66] Tsai CW, Lai SW, Cheng KH, Tsai MH, Davison A, Tsau CH, et al. Strong amorphization of high-entropy AlBCrSiTi nitride film. Thin Solid Films 2012;520:2613–8. http://dx.doi.org/10.1016/j.tsf.2011.11.025.

[67] Pogrebnjak AD, Beresnev VM, Smyrnova KV, Kravchenko YO, Zukowski PV, Bondarenko GG. The influence of nitrogen pressure on the fabrication of the two-phase superhard nanocomposite (TiZrNbAlYCr)N. Mater Lett 2018;211:316–8. http://dx.doi.org/10.1016/j.matlet.2017.09.121.

[68] Ay M, Schanzer C, Wolff M, Stahn J. New interface solution for Ni/Ti multilayers. Nucl instruments methods phys res sect a accel spectrometers. Detect Assoc Equip 2006;562:389–92. http://dx.doi.org/10.1016/j.nima.2006.02.188.

[69] Gopman DB, Dennis CL, Chen PJ, Iunin YL, Finkel P, Staruch M, et al. Strain-assisted magnetization reversal in Co/Ni multilayers with perpendicular magnetic anisotropy. Sci Rep 2016;6:1–8. http://dx.doi.org/10.1038/srep27774.

[70] Liu J, Barmak K. Interdiffusion in nanometric Fe/Ni multilayer films. J Vac Sci Technol A Vacuum, Surfaces, Film 2015;33. http://dx.doi.org/10.1116/1.4905465. 21510–21511-021510–4.

[71] Sun XH, Pan YP, Dong L, Zhao ML, Wan RX, Gu HQ, et al. Modulation period of Ag deposition on co-sputtered TiN-Ag leading to different microstructures: implication on mechanical properties and living cells growth. Surf Coating Technol 2017;326:382–7. http://dx.doi.org/10.1016/j.surfcoat.2016.10.040.

[72] Wu ZG, Zhang G a, Wang MX, Fan XY, Yan PX, Xu T. Structure and mechanical properties of Al/AlN multilayer with different AlN layer thickness. Appl Surf Sci 2006;253:2733–8. http://dx.doi.org/10.1016/j.apsusc.2006.05.039.

[73] Stone DS, Migas J, Martini A, Smith T, Muratore C, Voevodin AA, et al. Adaptive NbN/Ag coatings for high temperature tribological applications. Surf Coating Technol 2012;206:4316–21. http://dx.doi.org/10.1016/j.surfcoat.2012.04.054.

[74] Ma G, Lin G, Gong S, Liu X, Sun G, Wu H. Mechanical and corrosive characteristics of Ta/TaN multilayer coatings. Vacuum 2013;89:244–8. http://dx.doi.org/10.1016/j.vacuum.2012.05.024.

[75] Zou C, Xie W, Shao L. Functional multi-layer solar spectral selective absorbing coatings of AlCrSiN/AlCrSiON/AlCrO for high temperature applications. Sol Energy Mater Sol Cells 2016;153:9–17. http://dx.doi.org/10.1016/j.solmat.2016.04.007.

[76] Meng GH, Lin X, Xie H, Yue TM, Ding X, Sun L, et al. The effect of Cu rejection in laser forming of AlCoCrCuFeNi/Mg composite coating. Mater Des 2016;108:157–67. http://dx.doi.org/10.1016/j.matdes.2016.06.094.

[77] Nyemchenko US, Beresnev VM, Gorban VF, Novikov VJ, Yaremenko OV. Comparing the tribological properties of the coatings (Ti-Hf-Zr-V-Nb-Ta)N and (Ti-Hf-Zr-V-Nb-Ta)N + DLC. J Nano- Electron Phys 2015;7:1–4.

[78] Firstov SA, Karpov MI, Korzhov VP, Gorban VF, Krapivka NA, Stroganova TS. Structure and properties of a laminated composite material made of high-entropy alloy with carbide and intermetallic hardening. Bull Russ Acad Sci Phys 2015;79:1122–9. http://dx.doi.org/10.3103/S1062873815090051.

[79] Bondarev AV, Kiryukhantsev-korneev PV, Sheveyko AN, Shtansky DV. Structure, tribological and electrochemical properties of low friction TiAlSiCN/MoSeC coatings. Appl Surf Sci 2015;327:253–61. http://dx.doi.org/10.1016/j.apsusc.2014.11.150.

[80] Oliver WC, Pharr GM. An improved technique for determining hardness and elastic modulus using load and displacement sensing indentation experiments. J Mater Res 1992;7:1564–83.

[81] Giannozzi P, Baroni S, Bonini N, Calandra M, Car R, Cavazzoni C, et al. QUANTUM ESPRESSO: a modular and open-source software project for quantum simulations of materials. J Phys Condens Matter 2009;21:1–19. http://dx.doi.org/10.1088/0953-8984/21/39/395502.

[82] Vanderbilt D. Soft self-consistent pseudopotentials in a generalized eigenvalue formalism. Phys Rev B 1990;41:7892–5. http://dx.doi.org/10.1103/PhysRevB.41.7892.

[83] Perdew JP, Burke K, Ernzerhof M. Generalized gradient approximation made simple. Phys Rev Lett 1996;77:3865–8. http://dx.doi.org/10.1103/PhysRevLett.77.3865.

[84] Billeter SR, Curioni A, Andreoni W. Efficient linear scaling geometry optimization and transition-state search for direct wavefunction optimization schemes in density functional theory using a plane-wave basis. Comput Mater Sci 2003;27:437–45. http://dx.doi.org/10.1016/S0927-0256(03)00043-0.

[85] Iatsunskyi I, Kempiński M, Jancelewicz M, Załęski K, Jurga S, Smyntyna V. Structural and XPS characterization of ALD Al2O3 coated porous silicon. Vacuum 2015;113:52–8. http://dx.doi.org/10.1016/j.vacuum.2014.12.015.

[86] Matsuoka M, Isotani S, Sucasaire W, Kuratani N, Ogata K. X-ray photoelectron spectroscopy analysis of zirconium nitride-like films prepared on Si(100) substrates by ion beam assisted deposition. Surf Coating Technol 2008;202:3129–35. http://dx.doi.org/10.1016/j.surfcoat.2007.11.019.

[87] Rodríguez RJ, García JA, Medrano A, Rico M, Sánchez R, Martínez R, et al. Tribological behaviour of hard coatings deposited by arc-evaporation PVD. Vacuum 2002;67:559–66. http://dx.doi.org/10.1016/S0042-207X(02)00248-8.

[88] Bertóti I. Characterization of nitride coatings by XPS. Surf Coating Technol 2002;151–152:194–203. http://dx.doi.org/10.1016/S0257-8972(01)01619-X.

[89] Olaya JJ, Huerta L, Rodil SE, Escamilla R. Superconducting niobium nitride films deposited by unbalanced magnetron sputtering. Thin Solid Films 2008;516:8768–73. http://dx.doi.org/10.1016/j.tsf.2008.06.065.

[90] Mirabal-Rojas R, Depablos-Rivera O, Gómez CL, Fonseca-Garcia A, Medina JC, Barrera-Ortega CC, et al. Reduction of the coefficient of friction of niobium nitride coatings by the addition of bismuth. Vacuum 2016;125:146–53. http://dx.doi.org/10.1016/j.vacuum.2015.12.016.

[91] Wang T, Zhang G, Ren S, Jiang B. Effect of nitrogen flow rate on structure and properties of Mon x coatings deposited by facing target sputtering. J Alloy Comp 2017;701:1–8. http://dx.doi.org/10.1016/j.jallcom.2017.01.077.

[92] Powder Diffraction Files: 065-0565 (TiN), 065-0961 (ZrN), 033-0592 (HfN), 049-1283 (TaN), 038–1155 (NbN), (International Center for Diffraction Data) PDF-2 n.d.

[93] Liu ZTY, Burton BP, Khare SV, Gall D. First-principles phase diagram calculations for the rocksalt-structure quasibinary systems TiN-ZrN, TiN-HfN and ZrN-HfN. J Phys Condens Matter 2017;29. http://dx.doi.org/10.1088/0953-8984/29/3/035401. 35401(1)-35401(11).

[94] Isaev EI, Simak SI, Abrikosov IA, Ahuja R, Vekilov YK, Katsnelson MI, et al. Phonon related properties of transition metals, their carbides, and nitrides: a first-principles study. J Appl Phys 2007;101. http://dx.doi.org/10.1063/1.2747230. 123519(1)-123519(8).

[95] Lai C, Tsai M, Lin S, Yeh J. Influence of substrate temperature on structure and mechanical, properties of multi-element (AlCrTaTiZr) N coatings. Surf Coating Technol 2007;201:6993–8. http://dx.doi.org/10.1016/j.surfcoat.2006.11.009.

[96] Stöber L, Konrath JP, Haberl V, Patocka F, Schneider M, Schmid U. Nitrogen incorporation in sputter deposited molybdenum nitride thin films. J Vac Sci Technol A Vacuum, Surfaces, Film 2016;34:21513. http://dx.doi.org/10.1116/1.4941141.

[97] Tsai D, Chang Z, Kuo B, Tsao C, Chen E, Shieu F. Influence of discharge power on the structural, electro-optical, and mechanical properties of (TiZrHf) N coatings. J Alloy Comp 2015;622:446–57. http://dx.doi.org/10.1016/j.jallcom.2014.10.073.

[98] Pogrebnjak AD, Ivashchenko VI, Skrynskyy PL, Bondar OV, Konarski P, Załęski K, et al. Experimental and theoretical studies of the physicochemical and mechanical properties of multi-layered TiN/SiC films: temperature effects on the nanocomposite structure. Compos B Eng 2018;142:85–94. http://dx.doi.org/10.1016/j.compositesb.2018.01.004.

[99] De Faoite D, Browne DJ, Chang-Díaz FR, Stanton KT. A review of the processing, composition, and temperature-dependent mechanical and thermal properties of dielectric technical ceramics. J Mater Sci 2012;47:4211–35. http://dx.doi.org/10.1007/s10853-011-6140-1.

[100] Hsieh MH, Tsai MH, Shen WJ, Yeh JW. Structure and properties of two Al-Cr-Nb-Si-Ti high-entropy nitride coatings. Surf Coating Technol 2013;221:118–23. http://dx.doi.org/10.1016/j.surfcoat.2013.01.036.

[101] Chang SY, Lin SY, Huang YC, Wu CL. Mechanical properties, deformation behaviors and interface adhesion of (AlCrTaTiZr)Nx multi-component coatings. Surf Coating Technol 2010;204:3307–14. http://dx.doi.org/10.1016/j.surfcoat.2010.03.041.

[102] Abadias G, Kanoun MB, Goumri-Said S, Koutsokeras L, Dub SN, Djemia P. Electronic structure and mechanical properties of ternary ZrTaN alloys studied by

A new type of (TiZrNbTaHf)N/MoN nanocomposite coating: Microstructure and properties depending on energy

ab initio calculations and thin-film growth experiments. Phys Rev B Condens Matter 2014:90. http://dx.doi.org/10.1103/PhysRevB.90.144107.

[103] Mizutani U. Hume-rothery rules for structurally complex alloy phases. Boca Raton: CRC Press, Taylor and Francis Group, LLC; 2011.

[104] Jauberteau I, Bessaudou A, Mayet R, Cornette J, Jauberteau J, Carles P, et al. Molybdenum nitride films: crystal structures, synthesis, mechanical, electrical and some other properties. Coatings 2015;5:656–87. http://dx.doi.org/10.3390/coatings5040656.

[105] Jauberteau I, Mayet R, Cornette J, Bessaudou A, Carles P, Jauberteau JL, et al. A reduction-nitridation process of molybdenum films in expanding microwave plasma: crystal structure of molybdenum nitrides. Surf Coating Technol 2015;270:77–85. http://dx.doi.org/10.1016/j.surfcoat.2015.03.018.

[106] Bull CL, Kawashima T, McMillan PF, Machon D, Shebanova O, Daisenberger D, et al. Crystal structure and high-pressure properties of γ-Mo2N determined by neutron powder diffraction and X-ray diffraction. J Solid State Chem 2006;179:1762–7. http://dx.doi.org/10.1016/j.jssc.2006.03.011.

[107] Ihara H, Kimura Y, Senzaki K, Kezuka H, Hirabayashi M. Electronic structures of B1 Mon, fcc Mo2N, and hexagonal Mon. Phys Rev B 1985;31:3177–8. http://dx.doi.org/10.1103/PhysRevB.31.3177.

[108] Stöber L, Konrath JP, Krivec S, Patocka F, Schwarz S, Bittner A, et al. Impact of sputter deposition parameters on molybdenum nitride thin film properties. J Micromech Microeng 2015;25:1–11.

[109] Knotek O, Elsing R, Krämer G, Jungblut F. On the origin of compressive stress in PVD coatings - an explicative model. Surf Coating Technol 1991;46:265–74. http://dx.doi.org/10.1016/0257-8972(91)90169-W.

[110] Nouveau C, Djouadi M, Banakh O, Sanjinés R, Lévy F. Stress and structure profiles for chromium nitride coatings deposited by r.f. magnetron sputtering. Thin Solid Films 2001;398–399:490–5. http://dx.doi.org/10.1016/S0040-6090(01)01435-3.

[111] Jeong Heo S, Kim SW, Yeo IW, Park SJ, Oh YS. Effect of bias voltage on microstructure and phase evolution of Cr-Mo-N coatings by an arc bonded sputter system. Ceram Int 2016;42:5231–7. http://dx.doi.org/10.1016/j.ceramint.2015.12.048.

[112] Elmkhah H, Zhang TF, Abdollah-zadeh A, Kim KH, Mahboubi F. Surface characteristics for the Ti-Al-N coatings deposited by high power impulse magnetron sputtering technique at the different bias voltages. J Alloy Comp 2016;688:820–7. http://dx.doi.org/10.1016/j.jallcom.2016.07.013.

[113] Kim SK, Van Le V. Deposition of nanolayered CrN/AlBN thin films by cathodic arc deposition: influence of cathode arc current and bias voltage on the mechanical properties. Surf Coating Technol 2010;204:3941–6. http://dx.doi.org/10.1016/j.surfcoat.2009.12.011.

[114] Du H, Xiong J, Zhao H, Wu Y, Wan W, Wang L. Structure and properties of TiAlLaN films deposited at various bias voltages. Appl Surf Sci 2014;292:688–94. http://dx.doi.org/10.1016/j.apsusc.2013.12.035.

[115] Gangopadhyay S, Acharya R, Chattopadhyay AK, Paul S. Effect of substrate bias voltage on structural and mechanical properties of pulsed DC magnetron sputtered TiN-MoSx composite coatings. Vacuum 2010;84:843–50. http://dx.doi.org/10.1016/j.vacuum.2009.11.010.

[116] Ma Q, Li L, Xu Y, Gu J, Wang L, Xu Y. Effect of bias voltage on TiAlSiN nanocomposite coatings deposited by HiPIMS. Appl Surf Sci 2017;392:826–33. http://dx.doi.org/10.1016/j.apsusc.2016.09.028.

[117] Shen W-J, Tsai M-H, Chang Y-S, Yeh J-W. Effects of substrate bias on the structure and mechanical properties of (Al1.5CrNb0.5Si0.5Ti)Nx coatings. Thin Solid Films 2012;520:6183–8. http://dx.doi.org/10.1016/j.tsf.2012.06.002.

[118] Liu W, Li A, Wu H, He R, Huang J, Long Y, et al. Effects of bias voltage on microstructure, mechanical properties, and wear mechanism of novel quaternary (Ti, Al, Zr) N coating on the surface of silicon nitride ceramic cutting tool. Ceram Int 2016;42:17693–7. http://dx.doi.org/10.1016/j.ceramint.2016.08.089.

[119] Chang HW, Huang PK, Yeh JW, Davison A, Tsau CH, Yang CC. Influence of substrate bias, deposition temperature and post-deposition annealing on the structure and properties of multi-principal-component (AlCrMoSiTi)N coatings. Surf Coating Technol 2008;202:3360–6. http://dx.doi.org/10.1016/j.surfcoat.2007.12.014.

[120] Nita F, Mastail C, Abadias G. Three-dimensional kinetic Monte Carlo simulations of cubic transition metal nitride thin film growth. Phys Rev B 2016;93:1–13. http://dx.doi.org/10.1103/PhysRevB.93.064107.

[121] Gall D, Kodambaka S, Wall MA, Petrov I, Greene JE. Pathways of atomistic processes on TiN(001) and (111) surfaces during film growth: an ab initio study. J Appl Phys 2003;93:9086–94. http://dx.doi.org/10.1063/1.1567797.

[122] Abadias G. Stress and preferred orientation in nitride-based PVD coatings. Surf Coating Technol 2008;202:2223–35. http://dx.doi.org/10.1016/j.surfcoat.2007.08.029.

[123] Petrov I, Hultman L, Sundgren J-E, Greene JE. Polycrystalline TiN films deposited by reactive bias magnetron sputtering: effects of ion bombardment on resputtering rates, film composition, and microstructure. J Vac Sci Technol A Vacuum, Surfaces, Film 1992;10:265–72. http://dx.doi.org/10.1116/1.578074.

[124] Pelleg J, Zevin LZ, Lungo S, Croitoru N. Reactive-sputter-deposited TiN films on glass substrates. Thin Solid Films 1991;197:117–28. http://dx.doi.org/10.1016/0040-6090(91)90225-M.

[125] Shetty AR, Karimi A. Texture change through film thickness and off-axis accommodation of (0 0 2) planes. Appl Surf Sci 2011;258:1630–8. http://dx.doi.org/10.1016/j.apsusc.2011.10.037.

[126] Iordanova I, Kelly P, Mirchev R, Antonov V. Crystallography of magnetron sputtered TiN coatings on steel substrates. Vacuum 2007;81:830–42. http://dx.doi.org/10.1016/j.vacuum.2006.09.018.

[127] Abadias G, Tse YY, Guérin P, Pelosin V. Interdependence between stress, preferred orientation, and surface morphology of nanocrystalline TiN thin films deposited by dual ion beam sputtering. J Appl Phys 2006;99. http://dx.doi.org/10.1063/1.2197287. 113519(1)-113519(13).

[128] Patsalas P, Gravalidis C, Logothetidis S. Surface kinetics and subplantation phenomena affecting the texture, morphology, stress, and growth evolution of titanium nitride films. J Appl Phys 2004;96:6234–5. http://dx.doi.org/10.1063/1.1811389.

[129] Schell N, Matz W, Bøttiger J, Chevallier J, Kringhøj P. Development of texture in TiN films by use of in situ synchrotron x-ray scattering. J Appl Phys 2002;91:2037–44. http://dx.doi.org/10.1063/1.1436558.

[130] Yate L, Emerson Coy L, Wang G, Beltrán M, Díaz-Barriga E, Saucedo EM, et al. Tailoring mechanical properties and electrical conductivity of flexible niobium carbide nanocomposite thin films. RSC Adv 2014;4:61355–62. http://dx.doi.org/10.1039/C4RA11292J.

[131] Beake BD, Vishnyakov VM, Harris AJ. Relationship between mechanical properties of thin nitride-based films and their behaviour in nano-scratch tests. Tribiology Int 2011;44:468–75. http://dx.doi.org/10.1016/j.triboint.2010.12.002.

[132] Musil J, Jirout M. Toughness of hard nanostructured ceramic thin films. Surf Coating Technol 2007;201:5148–52. http://dx.doi.org/10.1016/j.surfcoat.2006.07.020.